Numerical Simulation of Cyclone Sidr Using a Cloud-Resolving Model: Characteristics and Formation Process of an Outer Rainband

NASREEN AKTER

Hydrospheric Atmospheric Research Center, Nagoya University, Nagoya, Japan, and Department of Physics, Bangladesh University of Engineering and Technology, Dhaka, Bangladesh

KAZUHISA TSUBOKI

Hydrospheric Atmospheric Research Center, Nagoya University, Nagoya, and Frontier Research Center for Global Change, Yokohama, Japan

ABSTRACT

Cyclone Sidr, one of the most devastating tropical cyclones that resulted in several thousand deaths and substantial damages, developed in the north Indian Ocean and made landfall over the Bangladesh coast on 15 November 2007. Observation and simulation results show that Sidr was embedded in a nonuniform environment and contained an intense outer rainband to the east of its center and a significant frontal band to the northwest. A detailed study of the outer rainband is performed by numerical simulation.

The eastern band was a long, quasi-straight shape in the meridional direction that remained stationary relative to the cyclone center. This band was composed of convective cells that developed southeast of the center within a synoptic-scale convergence zone and propagated along the band toward the northeast quadrant. The speed of the downwind-propagating cells was greater than that of the cyclone, which resulted in a convective cluster northeast of the center. Only the downwind portion of the band consisted of convection with stratiform rain, whereas the upwind and middle portions contained active convective cells without stratiform rain.

The band was located between the synoptic-scale flows of a weakly sheared, gradient-balanced westerly and a strongly sheared, nongradient-balanced prevailing southerly caused by the complex terrain of the Bay of Bengal's southeast region. Low-level convergence along the band was dominated by cross-band flow from both sides of the band and was confined below 3 km. As the cyclone moved northward, the convergence zone resulted in the extension of band length up to ~800 km. The southerly at the eastern side of the center gradually accelerated and was directed toward the center by a strong pressure gradient force. The flow accumulated a substantial amount of water vapor from the sea in addition to the increased moisture in the lower troposphere, resulting in further intensification of the convective cells.

1. Introduction

Rainbands are distinguishable features of tropical cyclones (TCs) that contribute to the total amount of rainfall and play an important role in the dynamics and intensity of TCs (Willoughby et al. 1982; Barnes et al. 1983; Powell 1990b; May and Holland 1999; Wang 2002a, 2009). Rainbands are categorized as inner or outer and stationary or moving on the basis of their relative positions and propagation to the cyclone center, respectively. Inner rainbands lie close to the vortex center, and outer rainbands develop at a distance of 80–150 km (Wang 2002a) or more (Willoughby et al. 1984; Skwira et al. 2005) from the center. Willoughby et al. (1984) identified the relatively motionless type of outer rainband as a stationary band complex (SBC), which consists of one principal band and several secondary bands on its concave side. Skwira et al. (2005) classified the rainband located outside the principal band as the outer rainband.

The horizontal shape of an outer rainband is generally prominent with equiangular spiral geometry (Senn et al. 1957). These bands consist of convective cells embedded in a large region of stratiform precipitation with varied

Corresponding author address: Nasreen Akter, Hydrospheric Atmospheric Research Center, Nagoya University, Nagoya 464-8601, Japan.
E-mail: akter@rain.hyarc.nagoya-u.ac.jp

organization. Several studies showed that the bands are more convective at the upwind portion, whereas the downwind portion consists of decaying convective cells with dominating stratiform precipitation (e.g., Barnes et al. 1983; Hence and Houze 2008). Alternatively, Barnes et al. (1991) and Ryan et al. (1992) documented a random arrangement of along-band cellular convections. In most studies, convective cells are reportedly located on the concave (inner) side with stratiform rain on the convex (outer) side within the bands (e.g., Willoughby et al. 1984; Powell 1990a; Hence and Houze 2008).

Most of the early theories suggest that the outer bands were inertia–gravity waves (Kurihara 1976; Diercks and Anthes 1976; Willoughby 1978) generated by latent heat release. According to Willoughby et al. (1984), the principal outer rainband is an outcome of low-level convergence caused by the interaction of the vortex movement with its environment. Recent studies have revealed the importance of downdrafts in the evolution of outer rainbands (e.g., Tabata et al. 1992; Powell 1990a; Nasuno and Yamasaki 1997; Murata et al. 2003; Wang 2002b; Didlake and Houze 2009). Low-level convergence occurs in the outer rainband mainly through interaction between the inflow and cold air associated with the downdraft. The convective downdraft blocks the radial inflow, which reinforces the low-level updraft motion. In some cases, inflow originates from the convex (outer) side of the band (Powell 1990a; Murata et al. 2003), while in other cases, it develops in the concave (inner) side of the band (Ishihara et al. 1986; Tabata et al. 1992).

Because the formation mechanisms of outer rainbands vary in TCs, the objective of the present research is to study the outer rainband of Cyclone Sidr (2007), which was one of the strongest TCs ever recorded in the Bay of Bengal of the north Indian Ocean (NIO). Sidr contained two long, intense rainbands that extended in the north–south direction (Fig. 1). To our knowledge, no study has reported on the detailed structures, positions, and formations of rainbands in NIO cyclones.

The regional monsoon circulation has a significant impact on the formation and subsequent motion of TCs, as summarized by Harr and Chan (2005). The NIO is influenced by the South Asian monsoon circulation resulting from land–ocean thermal contrasts and orographic features (Das 1968; Wang 2006). The South Asian monsoon is characterized by a warm, moist southwesterly low-level flow during the summer and a cool, dry northeasterly low-level flow during the winter (Shankar et al. 2002). In general, no TC activity occurs in the NIO during the summer monsoon period, while distinct bimodal peaks are found in the premonsoon (especially May) and postmonsoon (November) seasons (Alam et al. 2003; Krishna 2008). Most studies have noted the impact of

monsoons and the effects of their interannual and intraseasonal variabilities on TC activities in addition to the recurving of their tracks in various basins (Chen et al. 1998, 2004; Chan 2000; Wang and Chan 2002; Harr and Chan 2005; Cheung 2006) including the Bay of Bengal (Choudhury 1994; Singh et al. 2000). Few studies have discussed the formation of deep convection over the Bay of Bengal caused by the monsoon flow effect (Roca and Ramanathan 2000; Bhat et al. 2001; Zuidema 2003). Therefore, in the present study, the characteristics of Cyclone Sidr's outer rainband are explained with respect to the following details: (i) horizontal shape, (ii) structure, and (iii) formation process and maintenance. To study these features, the characteristics of the environmental flow in the Bay of Bengal and their effects on rainbands are investigated because this region is sensitive to both synoptic-scale monsoon flow and the flow patterns induced by its surrounding complex terrain.

During the approach of Cyclone Sidr, only a single 440-km-range Doppler radar was in operation over the entire coast. Because the plan position indicator (PPI) image data are not sufficient for analyzing the formation of rainbands over the ocean, a numerical model is necessary for studying the problem. In the present study, a numerical simulation with a 2.5-km horizontal resolution was performed using the Cloud Resolving Storm Simulator (CReSS) model (Tsuboki and Sakakibara 2002; 2007) in order to study cloud-scale structures of the rainband and their interactions with the synoptic-scale environment.

2. Numerical model and experimental setup

The numerical model CReSS, a three-dimensional, nonhydrostatic, and compressible cloud-resolving model developed at the Hydrospheric Atmospheric Research Center of Nagoya University, was used to simulate Cyclone Sidr. The CReSS model has successfully simulated numerous atmospheric phenomena (Liu et al. 2004; Wang et al. 2005; Maesaka et al. 2006; Ohigashi and Tsuboki 2007; Yamada 2008) including TCs (Tsuboki and Sakakibara 2007). The model's basic equations were solved in the terrain-following coordinates with prognostic variables for three-dimensional velocity components, perturbation of potential temperature, perturbation pressure, subgrid-scale turbulent kinetic energy (TKE), and mixing ratios for water vapor and hydrometeors. The finite-difference method was used for spatial discretization. The model was designed with various physical parameterization schemes, which are detailed by Tsuboki and Sakakibara (2002, 2007). Convection was resolved explicitly with no cumulus parameterization.
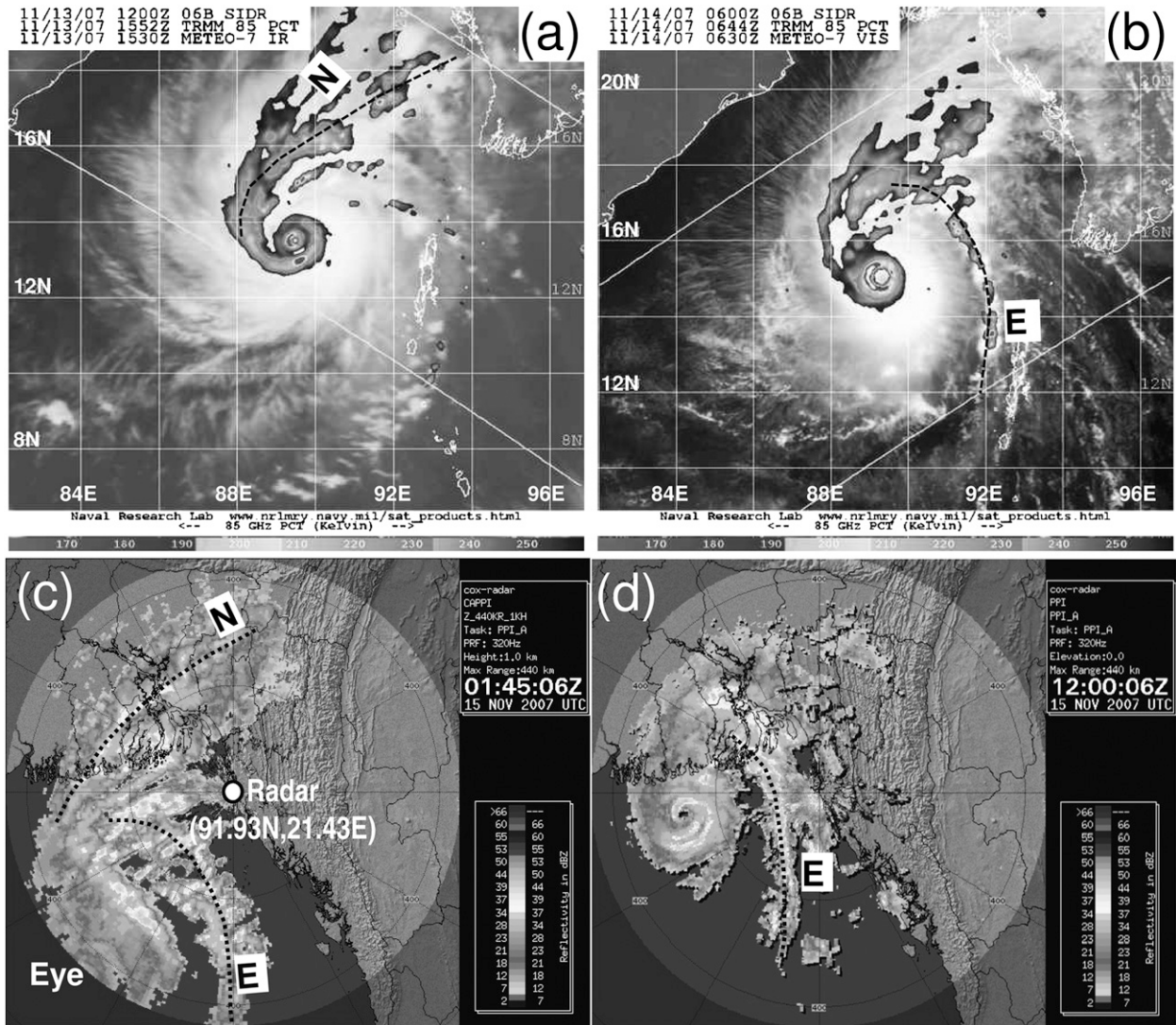
FIG. 1. TRMM 85-GHz PCT images at (a) 1552 UTC 13 Nov and (b) 0644 UTC 14 Nov 2007, superimposed on nearby-time Meteosat image of Cyclone Sidr. Radar CAPPI reflectivity images at 1-km height for (c) 0145 UTC 15 Nov and (d) 1200 UTC 15 Nov 2007. In all images, dotted lines indicate cloud and rainbands. The N and E indicate the northern and eastern bands, respectively.

In the present study, the CReSS model was used to cover a horizontal computational domain of 1500 km × 1575 km, indicated by the dotted box in Fig. 2. The domain consisted of 600 × 630 × 60 grid points on the Lambert conformal projection. The horizontal resolution was 2.5 km, and the vertical grid was stretched with variation from 100 m at the lowest level to 564 m at the top level. The upper boundary condition was rigid. The region above 21 km was set to be a sponge layer that damps vertically propagating waves. The wave-radiating boundary condition using constant phase velocity was used at the lateral boundaries. The bulk cold-rain microphysical scheme was used for the moist process. This parameterization contains both prognostic equations for

the mixing ratio of water vapor, cloud ice, rain, snow, and graupel, and the number densities of cloud ice, snow, and graupel. The subgrid turbulence was parameterized with 1.5-order closure with TKE. The radiation process was considered only in the heat balance at the surface. The surface scheme included a bulk method (Louis et al. 1981) for calculating ground and sea surface temperatures using a one-dimensional heat diffusion equation.

Global spectral model (GSM) data at 6-h intervals and 0.5° × 0.5° resolutions provided by the Japan Meteorological Agency (JMA) were applied for the atmospheric initial and lateral boundary conditions. No bogus vortex was included in the initial condition to perform the simulation of Cyclone Sidr. The daily sea
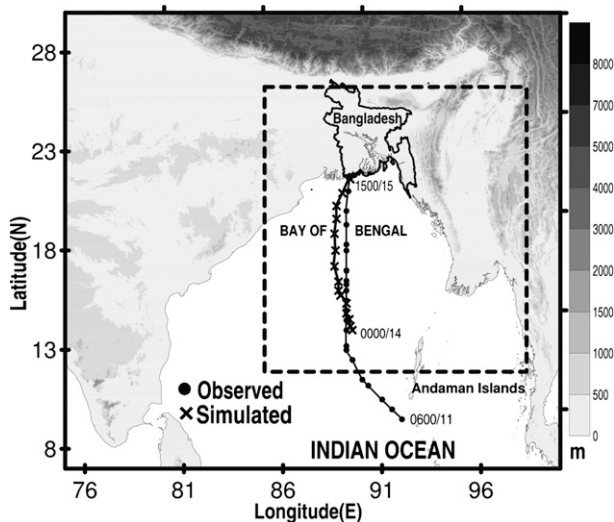
FIG. 2. The dashed box represents the domain for simulation. Lines with dots and crosses indicate the observed and simulated tracks, respectively, of Cyclone Sidr at 3-h intervals.

surface temperature (SST) product, the Merged satellite and in situ data Global Daily SST (MGDSST) of JMA with 0.25° resolution (Sakurai et al. 2005) were used for the lower boundary condition over water. The model was executed for a period of 48 h from 0000 UTC 14 November to 0000 UTC 16 November 2007.

3. Overview of Cyclone Sidr

Cyclone Sidr initially formed as a weak, low-level disturbance just southeast of the Andaman Islands in the NIO on 9 November 2007. The disturbance intensified quickly, moved slowly northwestward into the Bay of Bengal, headed northward, and finally, made landfall at the Bangladesh coast as a very severe cyclone (category 4 equivalent) at approximately 1500 UTC 15 November. After the landfall, it weakened rapidly and dissipated the next day. The maximum wind speed of Cyclone Sidr was 69 m s^{-1}, and its lowest central pressure before the landfall was 944 hPa (Hasegawa 2008). Its diameter was ~450 km with a cloud height of 13–15 km (Mukhopadhyay and Dutta 2007), and it caused a storm surge of ~5 m. According to the assessment by the Bangladesh Water Development Board, Cyclone Sidr is one of the 10 strongest cyclones to hit Bangladesh in the last 132 years, recorded from 1876 to 2007 (Hasegawa 2008). The cyclone resulted in severe casualties, affecting 8.9 million people and causing 3363 deaths, 871 missing persons, and 10 007.65 km^2 of damaged crops. The estimated economic loss was more than $3.1 billion (U.S. dollars).

The available satellite and radar observations of Cyclone Sidr reveal convective cloud–rainbands spiraling

into its eyewall. The cloud bands in Figs. 1a,b are represented by composite images of the Tropical Rainfall Measuring Mission (TRMM) and the European Organization's *Meteosat-7* satellites for 13 and 14 November, respectively. In Figs. 1c,d, the constant altitude plan position indicator (CAPPI) images of radar reflectivity illustrate the rainbands. Cyclone Sidr contained two long, prominent rainbands: one on the eastern side of the eye elongated toward the south (the eastern band) and the other to the west of the eye extended to the north (the northern band). The northern band appeared early during the cyclone, whereas the eastern band developed with cyclone intensification (Figs. 1a,b). However, the exact time of the first appearance of the bands is not available because of discontinuity of observed data.

4. Results

a. Validation of simulated Cyclone Sidr

The low-level structure of the TC is represented in Fig. 3 by the horizontal distributions of the variables of sea level pressure, surface wind, and precipitation for three instances of the simulation. The eyewall was located almost 25 km from the center with two long, quasi-straight major bands placed >150 km away from the center on each side extending in the north–south direction. The cyclone moved northward accompanying both the rainbands and gradually intensified until the landfall. The simulated Cyclone Sidr was verified using the available observed data as follows.

1) CYCLONE TRACK AND INTENSITY

The Bangladesh Meteorological Department (BMD) provided data on TC track and intensity, both of which were estimated by the BMD using the Dvorak method (Dvorak 1975). The lines with dots and crosses in Fig. 2 represent observed and simulated tracks of Sidr, respectively. The observed tracking period was from 0600 UTC 11 November to 1500 UTC 15 November; the simulation period was from 0000 UTC 14 November to 1500 UTC 15 November. The simulated cyclone positions were determined by the location of the minimum sea level pressure. The simulated track was fairly accurate with a root-mean-square error (RMSE) of 70 km when compared with the observed positions. Considering the BMD-recorded landfall location, the simulated landfall was ~2 h later than that of the observed cyclone (1500 UTC 15 November). However, the simulated cyclone landfall occurred at nearly the same location (eye position: 21.7°N, 89.5°E) on the coast as that of the observed cyclone (eye position: 21.7°N, 89.4°E). The average speed of the simulated cyclone
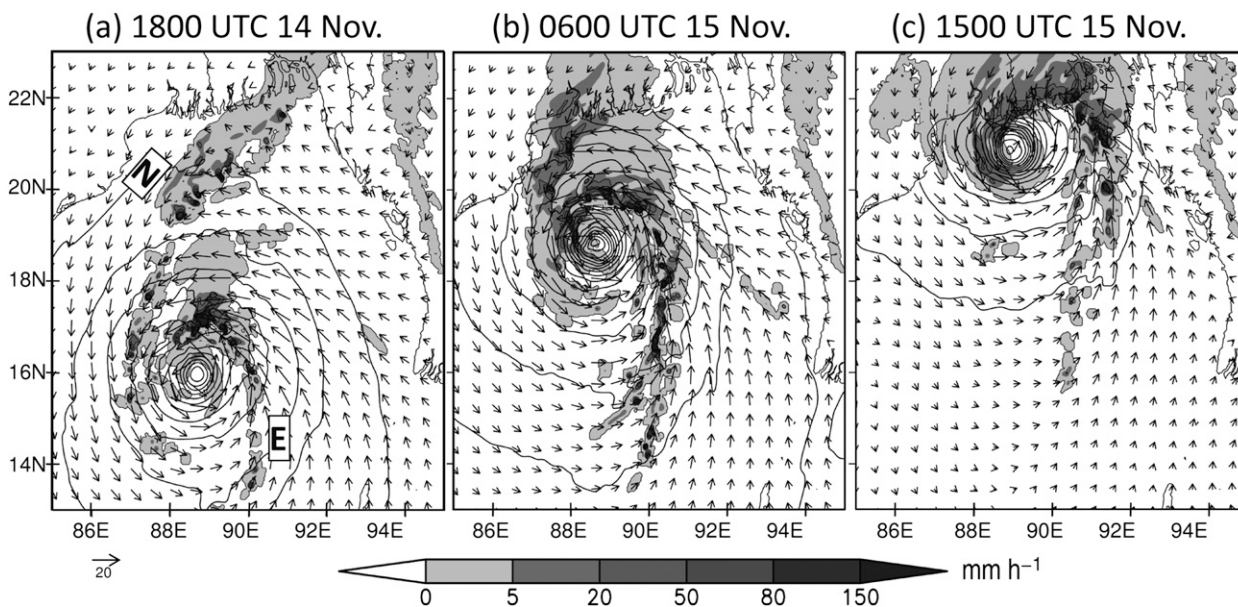
FIG. 3. Simulated results displaying rain rate (shading) in mm h^{-1}, sea level pressure (contour at 2-hPa interval), and surface wind (vector) in m s^{-1} at (a) 1800 UTC 14 Nov, (b) 0600 UTC 15 Nov, and (c) 1500 UTC 15 Nov 2007. The N and E in (a) indicate northern and eastern bands, respectively.

at 5.8 m s^{-1} was nearly the same as that of the observed value of 6.1 m s^{-1}.

Because the central pressure was not monitored continuously, we were unable to validate the simulated TC intensity with time. However, the minimum central pressure of 965 hPa in the simulation was higher than that of the observed value of 944 hPa. As a result, the simulated maximum wind speeds were lower than those estimated by the Dvorak technique by an average of 22 m s^{-1}. Furthermore, the maximum speed discrepancy occurred very close to the eye, which may not affect the analysis of outer rainbands and their formation mechanism in the present study. The simulated surface wind field at 0640 UTC 14 November (Fig. 4a) and 0550 UTC 15 November (Fig. 4c) was compared with the TRMM wind speed products at similar times (Figs. 4b,d). The results of the simulated wind speed near and around the northern and eastern bands showed values of 30–40 kt (~15.4–20.6 m s^{-1}), which were nearly equal to those of the observed data. In both simulation and observation, a remarkably strong southerly (Figs. 4c,d) was evident on the east side of the TC.

2) PRECIPITATION DISTRIBUTION

The simulated rainfall distribution pattern was validated with the reflectivity data collected from S-band (2850 MHz) Doppler radar of BMD placed at 21.43°N, 91.93°E. The radar, with a scan range of 0–440 km, was set 29.8 m above the ground and 360° in azimuth using a beamwidth of 1.46°. The gridded data resolutions were 1.375 km × 1.375 km in intensity mode and

0.625 km × 0.625 km in velocity mode. This radar provided CAPPI image at 1 km above ground level. Figure 5b shows the zero elevation PPI image of reflectivity at 1100 UTC 15 November, which can be compared to the rainfall simulated at the same time, as shown in Fig. 5a. The result represents a pattern of rainfall distribution similar to that observed in the radar image, except for precipitation on the eastern part of the eyewall. In both cases, the eastern band contained intense convective cells and a northern cluster with stratiform precipitation. In this study, convective cells are defined by the rain rate with a minimum threshold of 5 mm h^{-1} (~35 dBZ).

Further verification of the rainfall distribution pattern with satellite imagery is represented in Figs. 5c,d, which show the simulated and TRMM-observed rainfall rates, respectively. The TRMM polarization-corrected temperature (PCT) product in Fig. 5f shows a pattern similar to that of the simulated result in Fig. 5e. The model simulates both northern and eastern bands with long tail configurations. In the mature stage of the TC, the eastern band had a spatial extent ~800 km in length (Figs. 5e,f).

The BMD operates 31 rain gauges throughout the country, represented by crosses in Fig. 6, with data collected at 3-h intervals. For the quantitative verification of the total rainfall, the 3-h accumulated rain measured in millimeters at the rain gauge sites was extracted from the simulation for the period between 0000 UTC 15 November and 0000 UTC 16 November. The spatial distribution of the total simulated precipitation and rain gauge rainfall is shown in Fig. 6. The observation
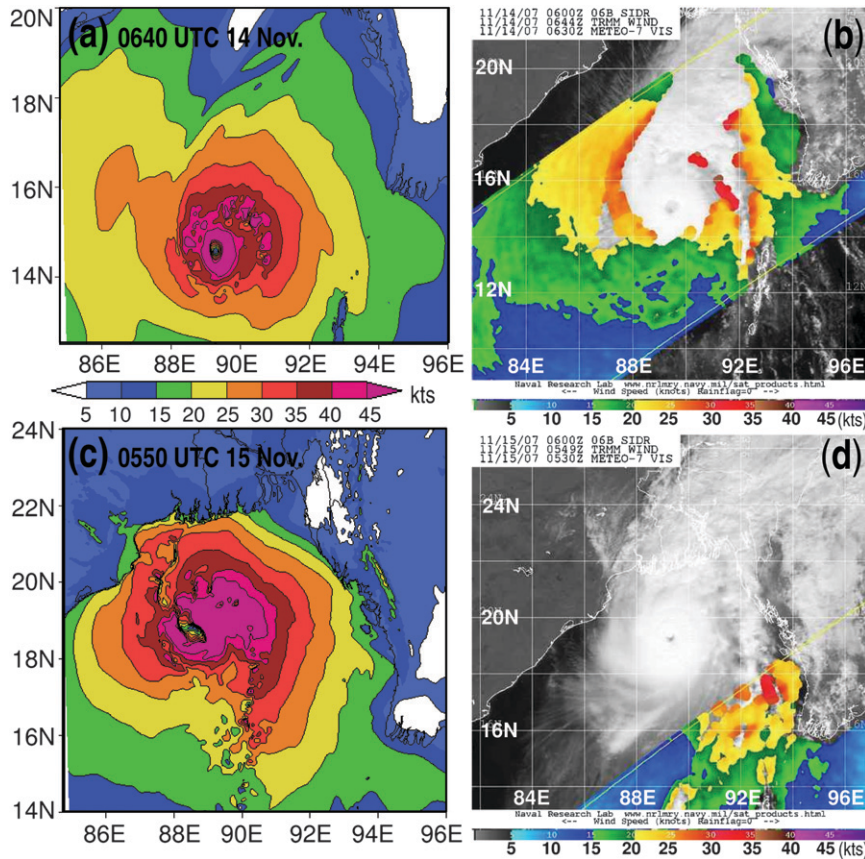
FIG. 4. Simulated surface horizontal wind speed (kt) at (a) 0640 UTC 14 Nov and (c) 0550 UTC 15 Nov 2007. TRMM wind speed image (color) in kt at (b) 0644 UTC 14 Nov and (d) 0549 UTC 15 Nov 2007 on nearby-time Meteosat imagery.

showed heavy distribution in the coastal region, gradually reducing in the land area away from the coast. Nearly the same distribution was represented in the simulation; however, the highest value was not exactly on the coast because the amount of rainfall simulated in the eastern side of the eyewall was lower than that observed. The correlation between the rain gauge data and the simulated rainfall was 0.68, which indicates a fair consistency. The RMSE of the simulated rainfall was 34.5 mm over the observed rainfall range of 0–150.8 mm.

3) THERMODYNAMIC ENVIRONMENT AROUND CYCLONE SIDR

The moisture in the environment of the simulated Cyclone Sidr at 2000 UTC 14 November was compared to a satellite image of precipitable water taken at nearly the same time (Figs. 7a,b). Although the model domain did not cover the entire satellite image area, a pattern of decreasing precipitable water (mm) from the east to the west of the cyclone was noted in both cases. The same pattern also appeared in the case of surface air temperature (Figs. 7c,d). The west side of the cyclone was cool and dry, whereas the east side was warm and moist.

The temperature gradient was significant along the northern band area, which is favorable for uplifting the air and creating convective clouds. It is evident that the northern band had a characteristic of a front. Conversely, the temperature gradient was insignificant in the eastern band region. Nevertheless, the convection was deeper in the eastern band region than in the northern band (not shown).

b. Simulated eastern rainband of Cyclone Sidr

1) HORIZONTAL SHAPE

The eastern band was oriented in the north–south direction. The longitudes of the cyclone center and the inner (western) edge of the eastern band at the latitude of the center (Fig. 8) show that throughout the simulation, the location of the band remained nearly stationary with respect to the center. The length of the simulated band observed at 3-h intervals indicated by shaded bars in Fig. 8 increased gradually to the south until the TC
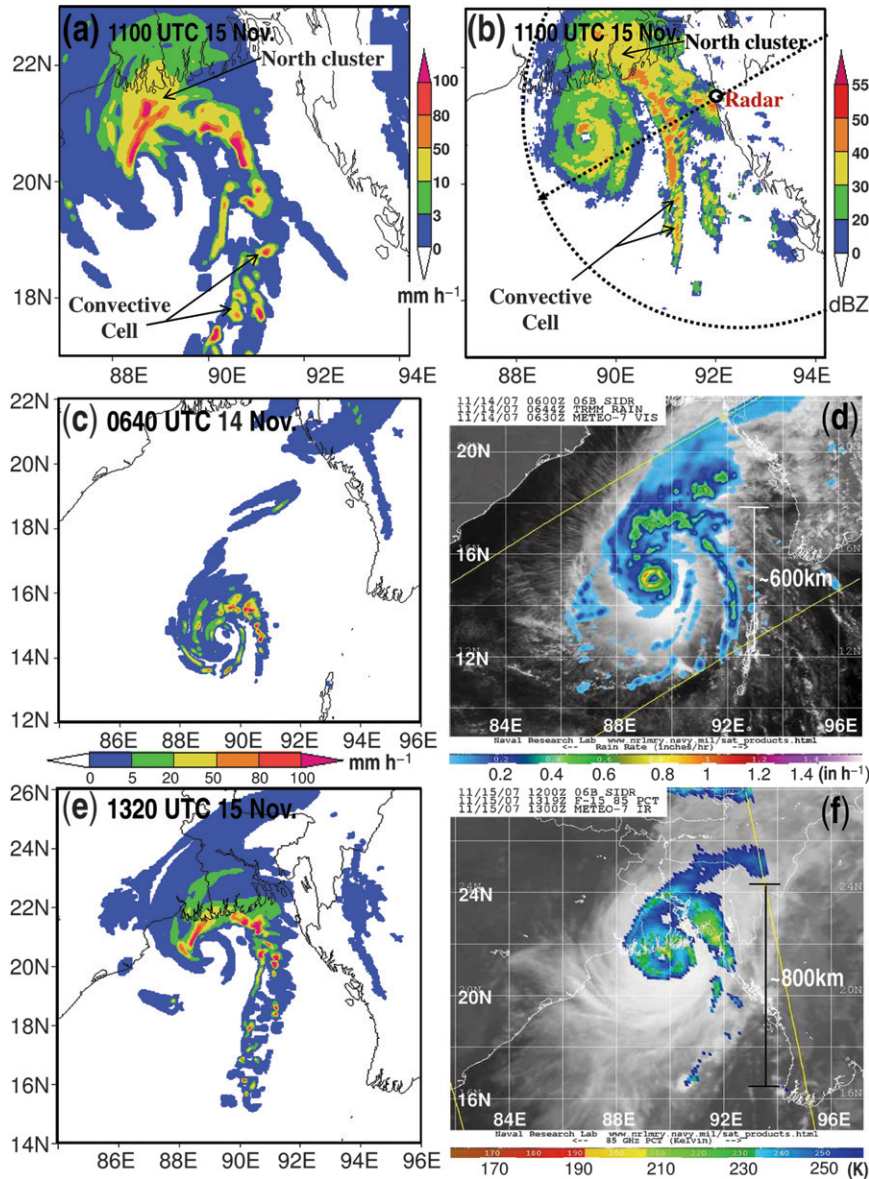
FIG. 5. (a) Simulated rain rate (mm h^{-1}) and (b) PPI images of radar reflectivity at 1100 UTC 15 Nov 2007. The position (21.43°N, 91.93°E) and range (440 km) of the radar are indicated by open and dotted circles, respectively. Simulated rain rate (mm h^{-1}) at (c) 0650 UTC 14 Nov and (e) 1320 UTC 15 Nov 2007. (d) TRMM rain rate (in h^{-1}) at 0644 UTC 14 Nov and (f) 85-GHz PCT (K) at 1319 UTC 15 Nov 2007 on nearby-time Meteosat images.

reached the mature stage. The band length was measured from the latitude of the TC center to the southernmost end of the rainband. The exact measurement of the length of the observed band could not be obtained because of the radar range limitation (Figs. 1c,d). However, the satellite images in Figs. 5d,f confirm an increase in band length with time. The relatively stationary position of the band at the eastern side of the cyclone was similar to the stationary principal outer rainband of

Willoughby et al. (1984), except that it exhibited a long, quasi-straight structure rather than a spiral structure.

2) ORGANIZATION AND KINEMATICS OF CELLS ALONG THE BAND

Cells in the band formed and organized along an area of intense moisture convergence ($\leq -10^{-3}$ g kg^{-1} s^{-1}). The shaded area in Fig. 9 represents the 3-h averaged field of surface moisture flux convergence (MFC) in
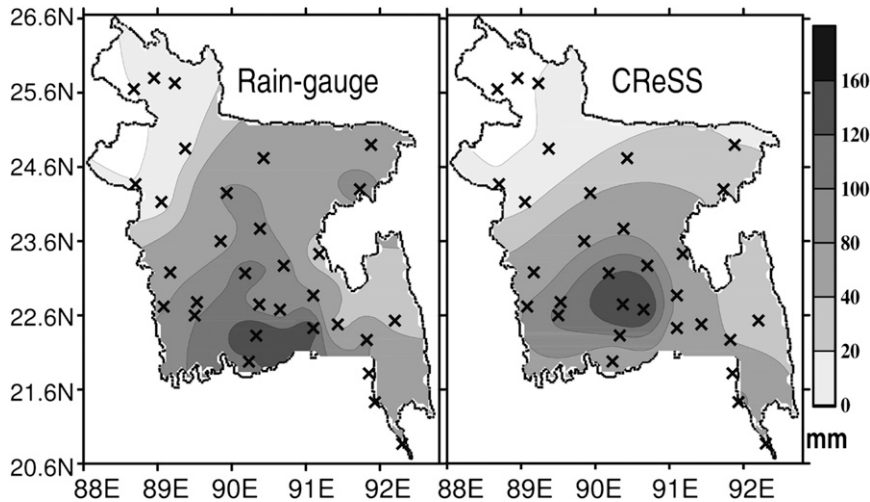
FIG. 6. Spatial distributions of total rain (mm) for the period from 0000 UTC 15 Nov to 0000 UTC 16 Nov 2007: (left) rain gauges and (right) CReSS. Crosses indicate rain gauge stations.

which spatial smoothing was applied to eliminate cloud-scale convergence. Smoothing was performed with a 9-point smoothing operator on gridded data, and its level was increased by repeating the procedure 5 times. During the period from 0600 UTC 14 November to 0600 UTC 15 November, the development of new convective cells with horizontal dimensions of approximately 10–15 km was examined at 10-min intervals. Within 24 h, a total of 54 cells formed; their positions are marked by circles in the figure. During this time, the low-level convergence along the eastern band increased gradually, particularly in the upwind (south) region, and most cells were arranged along the primary convergence line. Although most of the cells formed away from the TC center, their production was irregular in time and location; in contrast to most principal rainbands, whereby new cell development occurs along the upwind end (Didlake and Houze 2009).

At the times of cell formation, values of MFC ranged from -8 to -15×10^{-3} g kg^{-1} s^{-1} with horizontal divergence between -0.4 and -0.8×10^{-3} s^{-1}. Only nine cells developed with an MFC of approximately -10^{-4} g kg^{-1} s^{-1}. Convective initiation with MFC of $\leq -10^{-3}$ g kg^{-1} s^{-1} was observed in previous studies of severe storm cases (Ostby 1975; Negri and Vonder Haar 1980; Koch and McCarthy 1982; Beckman 1990; Rogash and Smith 2000). However, MFC is a highly scale-dependent storm predictor (Petterssen 1956; van Zomeren and van Delden 2007). In a special observational network with a horizontal resolution of 2.5 km $\times$ 2.5 km and a time resolution of 5 min, Ulanski and Garstang (1978) measured the magnitude of horizontal divergence to be as high as -2.7×10^{-3} s^{-1} near the developing convective updrafts.

Thus, the mesoscale MFC and horizontal divergence produced a local environment favorable for intense cell development along the eastern band of Cyclone Sidr.

After formation, cells moved downwind (north) along the rainband, increasing in diameter, and finally joining to create a convective cluster northeast of the cyclone center (Fig. 5a). This cluster maintained a horizontal dimension of 100 $\sim$ 200 km or larger and merged with the eyewall of the cyclone. Because band development is directly related to cell generation in the upwind region and their relative speeds toward the downwind area, a detailed examination of the cluster characteristics was not performed in the present study.

The tangential and radial components of cell motion relative to the TC center, which are closely associated with band elongation, were analyzed for 54 cells. During the period from 0600 UTC 14 November to 0600 UTC 15 November, cell motions were calculated at 10-min intervals and averaged over their lifetime; specified here as the period from formation (5 mm h^{-1}) to either dissipation ($<$5 mm h^{-1}) or merger with the north cluster. In Fig. 10, the mean relative tangential and radial velocity components of cell motion are plotted with respect to distance from the cyclone center at the time of cell formation. The positive values of the tangential movement of the cells indicate that they moved faster than the TC center (Fig. 10a). Hence, they were able to overtake the eye and finally join the convective cloud cluster at the downwind end. Only 8 of 54 cells dissipated before merging with the cluster. A downward trend in tangential speed was observed ensuing high correlation (-0.66). Most cells displayed average inward radial movements with respect to the center (Fig. 10b). However,
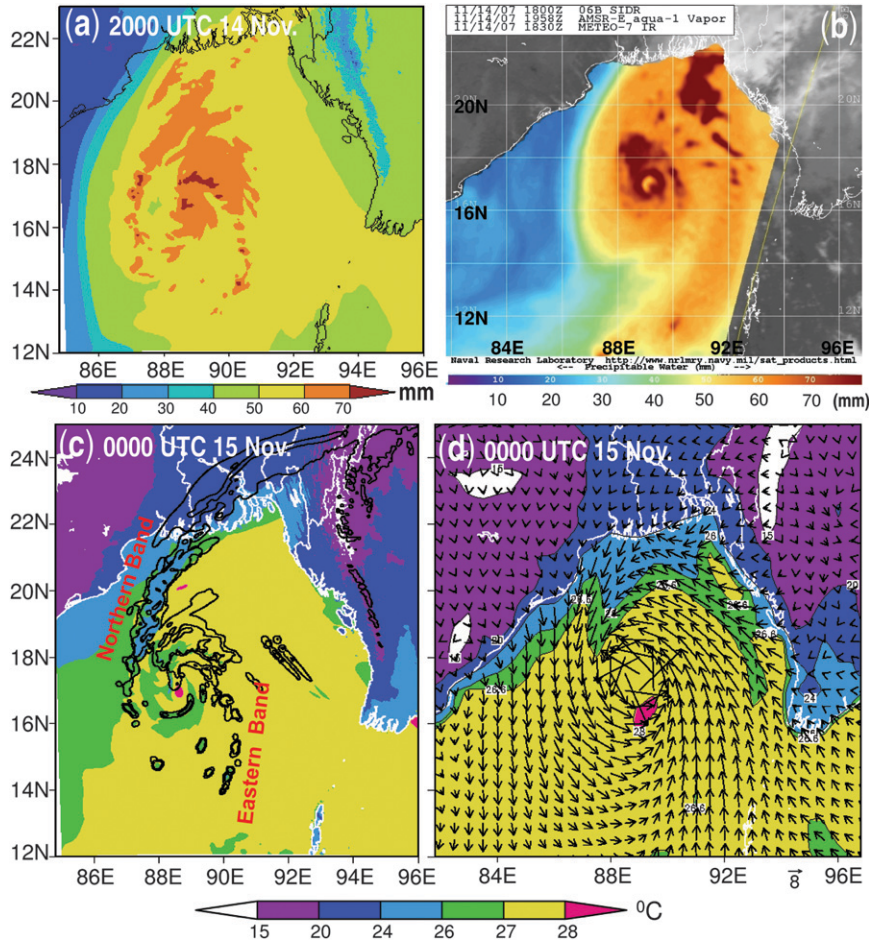
FIG. 7. Precipitable water (mm) of (a) simulated result at 2000 UTC 14 Nov and (b) *Aqua* satellite image obtained at 1958 UTC 14 Nov 2007. Surface temperature obtained from (c) the simulated result and (d) GSM data at 0000 UTC 15 Nov 2007. Contours of rain rate (mm h^{-1}) in (c) and surface wind vectors (m s^{-1}) in (d) were used to identify the band location and cyclone location, respectively.

relative radial movement did not have significant correlation (0.02) with the distance of cell formation. After formation, the cells propagated inward and northward from the eye; hence, the cells gradually moved in a spiral toward the center. The downwind propagation of the convective cells relative to the center resulted in a reduction in band length.

In addition, each individual cell's motion relative to the local mean wind of 0–6 km was calculated at the time of half-life of each cell, where the analyzed region was $0.5° \times 0.5°$, enclosing the cell. Most of the cells (44 out of 54) moved downwind with only a $\pm 10\%$ discrepancy from the mean wind, as shown in the scattered diagram of Fig. 10c. This cell movement is similar to that reported by Powell (1990a), in which cells in the rainbands of a hurricane were discovered to move at approximately 85% of the mean wind, which indicates ordinary convection.

Eight cells traveled slower (<80% of mean wind) and to the right of the mean wind, whereas only two cells moved to the left with higher speeds (>130% of mean wind). In most of the cases, the cells propagated in a clockwise curved-sheared environment. Hodographs for the movement of two representative cells are shown in Fig. 10d. One is a cell that moved along with the mean wind, and the other is a cell that moved slower (at 64%) of and to the right of the mean wind. These characteristics of the cells moving slowly and to the right of the strong clockwise vertical wind shear are consistent with supercell expectations (Weisman and Klemp 1984; Bunkers 2002). We recently investigated the detailed characteristics of several isolated convective cells along the eastern band and its associated environment with high-resolution (1-km grid spacing) simulation, in which the cells were discovered to be supercells with favorable
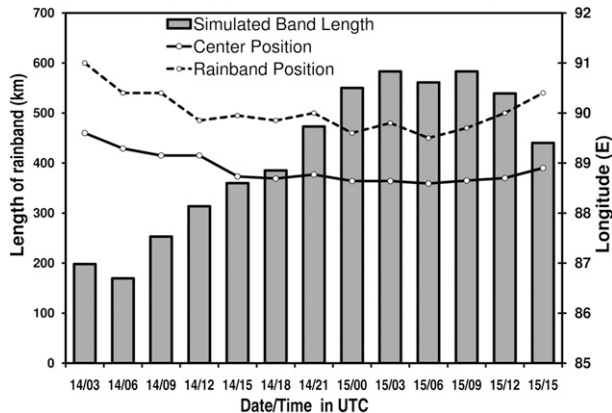
FIG. 8. Lines indicate the position of the eastern band with respect to the cyclone center. Shaded bars show simulated band length measured from the cyclone center at 3-h intervals from 0300 UTC 14 Nov to 1500 UTC 15 Nov 2007.

strong, clockwise vertical shear and storm-relative environmental helicity (Akter and Tsuboki 2010).

3) VERTICAL CHARACTERISTICS AND DEVELOPMENT PROCESS OF THE BAND

The band was divided into three regions in the along-band direction—downwind, middle, and upwind— each spanning 1.5° of latitude. Vertical cross sections at 0600 UTC (Fig. 11a) and 1200 UTC 15 November

(Fig. 11b) depict the meridional averages of precipitation, temperature perturbation, and the zonal and vertical components of wind velocity within each region of the band. The figure indicates that the upwind portion of the band was mostly convective, intensifying toward the middle part. The downwind portion had relatively weak convection along the inner edge of the band with stratiform precipitation on the outer side, which was also evident in the observation (Fig. 5b). This causes variation in bandwidth from ~20 km at the upwind end to ~200 km downwind. This along-band precipitation structure of Sidr is similar to that of the principal band (Barnes et al. 1983; Hence and Houze 2008). In the downwind region, the band was ~13 km high with an outward tilt. The upwind region of the band contained weak convection in the inner side (Fig. 11a); however, during the mature stage of the TC, the band had only one strong convective axis (Fig. 11b). The mean temperature perturbation from the background profile in each panel of Fig. 11 indicates weak or nonexistent cold pools near the convection.

Barnes et al. (1991) remarked that cold pools are the key feature that leads to upstream development of rainbands. However, cold pools are believed to be weak in the hurricane environment due to a lack of significant evaporation cooling (McCaul and Weisman 1996), compared to those often observed in midlatitude convection (Zipser 1977; Engerer et al. 2008). Many studies have
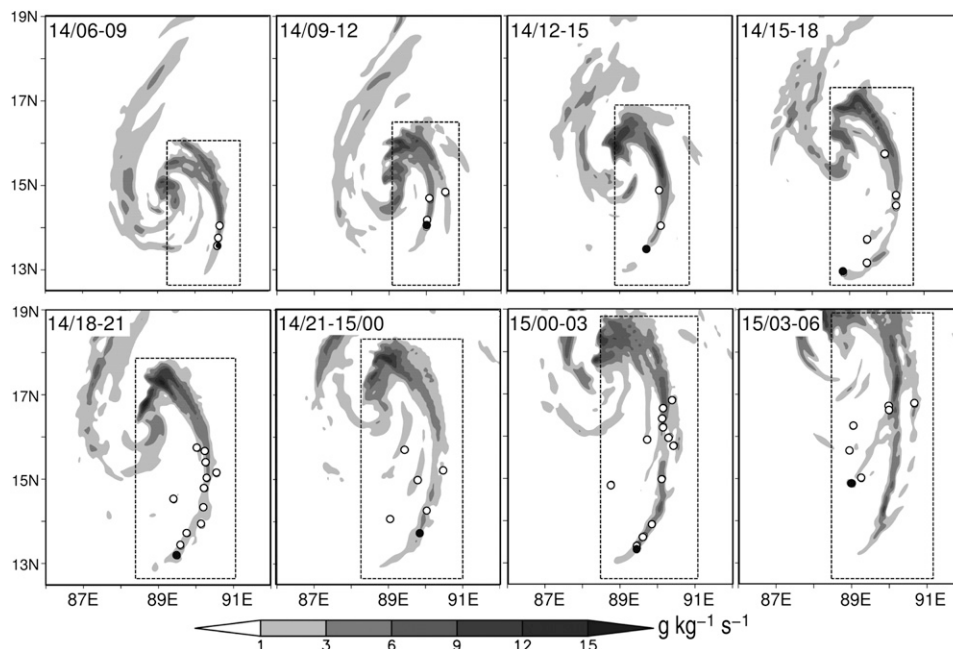

FIG. 9. Shading indicates 3-h-averaged smoothened surface moisture flux convergence (-10^{-3} g kg^{-1} s^{-1}), and the circle indicates the position of formation of the cells from (top left) 0600 UTC 14 Nov to (bottom right) 0600 UTC 15 Nov 2007. The closed circle represents the endmost cell. Dotted boxes indicate the observed areas for cell formation.
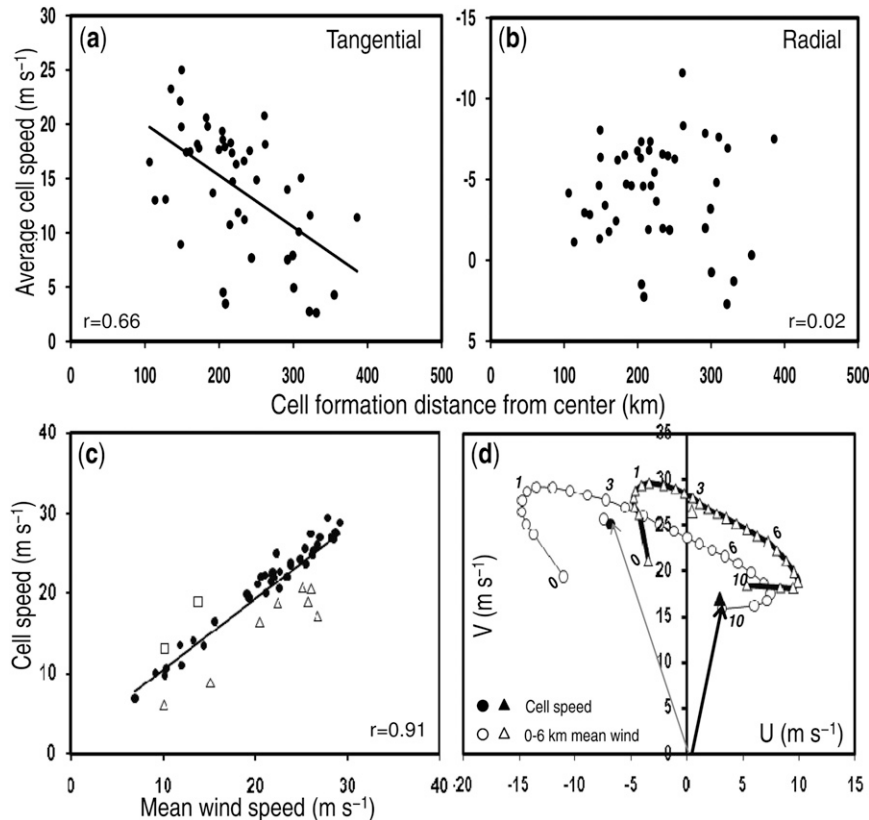
FIG. 10. Averaged (a) tangential and (b) radial movements of the cells with respect to the cyclone center plotted against the position of formation of the cells from the center. (c) Cell speed vs local mean (0–6 km) wind speed in m s^{-1}. Circular marks represent the cell motions with the mean wind, where triangular and rectangular marks indicate slow- and fast-moving cells, respectively. (d) Two hodographs from a $0.5° \times 0.5°$ analysis area; the thin line with a circle represents a cell motion with the mean wind at 1930 UTC 14 Nov and thick line with a triangle shows the slow moving cell at 0340 UTC 15 Nov 2007. Arrows represent cell motion. Numbers along the curves indicate height in km.

documented the existence of cold pools in rainbands in which the surface air was >2 K colder than that of the surrounding environment (e.g., Barnes et al. 1983; Yamasaki 1983; Powell 1990a; Eastin et al. 2012). In the present case, we examined the temperature deficiency around the new forming cells along the band. Figure 12 shows the surface potential temperature θ, updraft at 2-km height, downdraft at the surface, and surface horizontal wind for the most upwind cells of Fig. 9, indicated by closed circles in each panel. No significant temperature gradient was detected around the cells, which could favor cell uplifting. We discovered considerably weak and occasional cold air ($\Delta\theta < 1$ K) associated with the downdraft (<1 m s^{-1}), which formed beneath the matured cell (bottom-right panel: splitting the cell with two updraft cores) and confined to the cloud scale. The spread of weak cold air was insufficient for developing new cells along the upwind edge of the cold pool, which contrasts

with the development process of upwind growth of convection in spiral bands (e.g., Didlake and Houze 2009).

In the present case, a strong moist southerly on the outer side of the cyclone was critical to the formation and maintenance of the cells during the advancement of the cyclone to the north. Figure 13a shows the surface moisture flux vector and moisture flux convergence at 0300 UTC 15 November. Here the flow from the inner (western) side of the band produced convergence with the flow that originated from the outer (eastern) side. The southerly originated outside of the computational domain and transported more water vapor than the flow from the inner side of the band. In the region of persistent moisture convergence, convective instability—represented by surface-based convective available potential energy (CAPE; Fig. 13b)—resulted in the development of convective cells in the band. The highest CAPE, with a value of ~2000 J kg^{-1}, was observed along the eastern
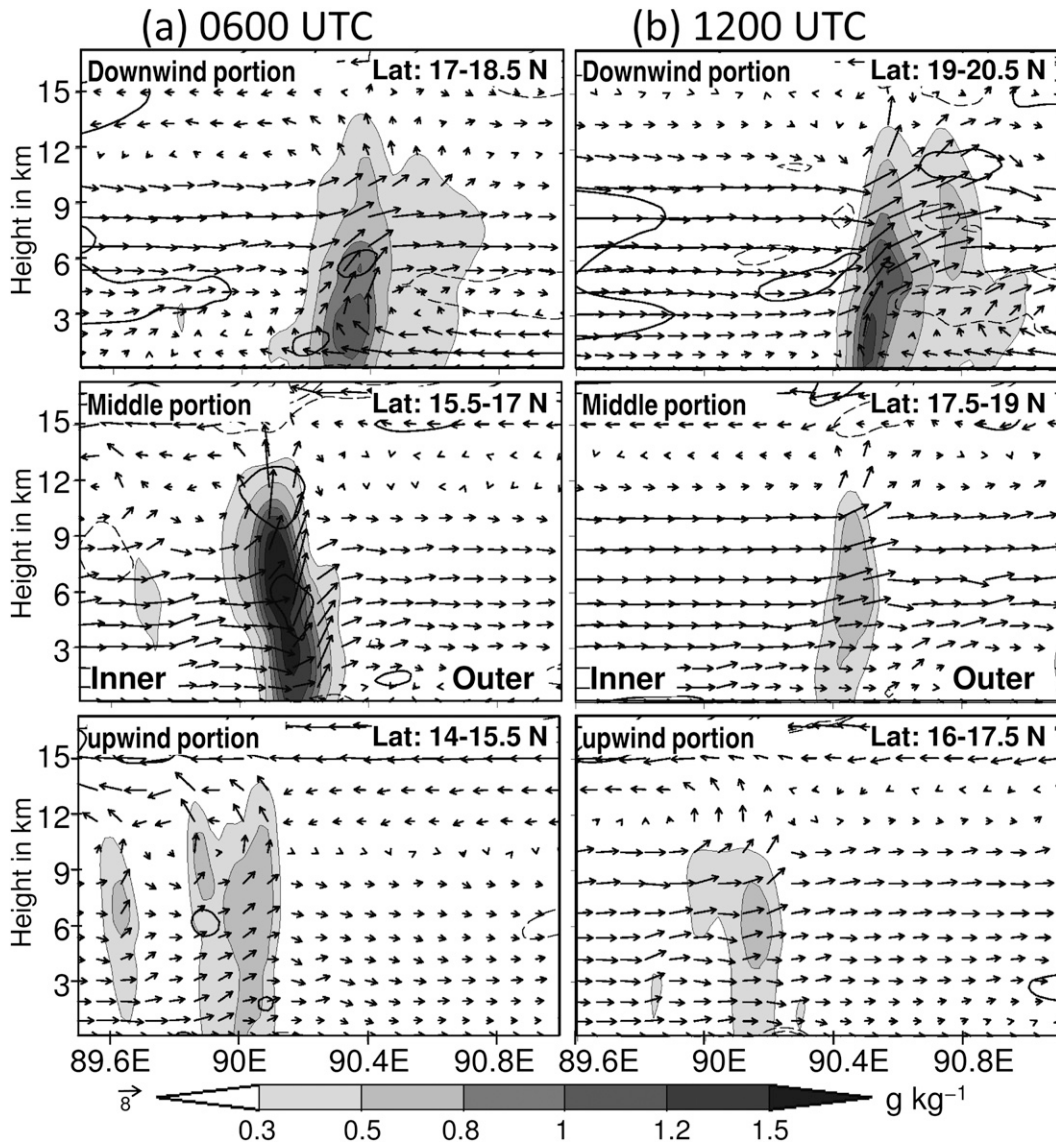
FIG. 11. Each panel represents 1.5° averaged vertical structures of total mixing ratio (rain, snow, and graupel) in g kg^{-1} (shading), solid and dash contours (interval of 0.4°C) indicate positive and negative temperature perturbation, and vectors indicate zonal and vertical velocity in m s^{-1} at (a) 0600 UTC 15 Nov and (b)1200 UTC 15 Nov 2007: (top) downwind, (middle) middle, and (bottom) upwind portion.

band and indicates a supportive environment for convection with strong updraft (McCaul 1991; McCaul and Weisman 2001; Baker et al. 2009). In addition, the hodographs (Fig. 14) plotted for the averaged area of the inner side (14°–17°N, 85.5°–89°E) and the outer side (14°–17°N, 90.5°–94°E) of the band (cf. Fig. 13a) allowed for the differences in characteristics between the flows from the inner and outer sides to be traced. The 0–6-km bulk (total) shear was 10.2 (21.4) m s^{-1} for the outer-side flow and 4.9 (11.7) m s^{-1} for the inner side. Bunkers (2002) specified that supercell initiation in environments is characterized by 10–15 m s^{-1} bulk shear and 20–25 m s^{-1}

total shear over the lowest 6 km. In accordance with this, the outer-side band environment displayed significant wind shear with stronger clockwise veering than did the inner side. The band was confined to the boundary of strongly directional sheared and little or no sheared environments.

Figure 15a displays the horizontal divergence [$(\partial u/\partial x) + (\partial v/\partial y)$], zonal[1] or cross-band flow gradient ($\partial u/\partial x$), and

---

[1] Zonal flow is roughly cross-band flow because of the band's quasi-north–south orientation.
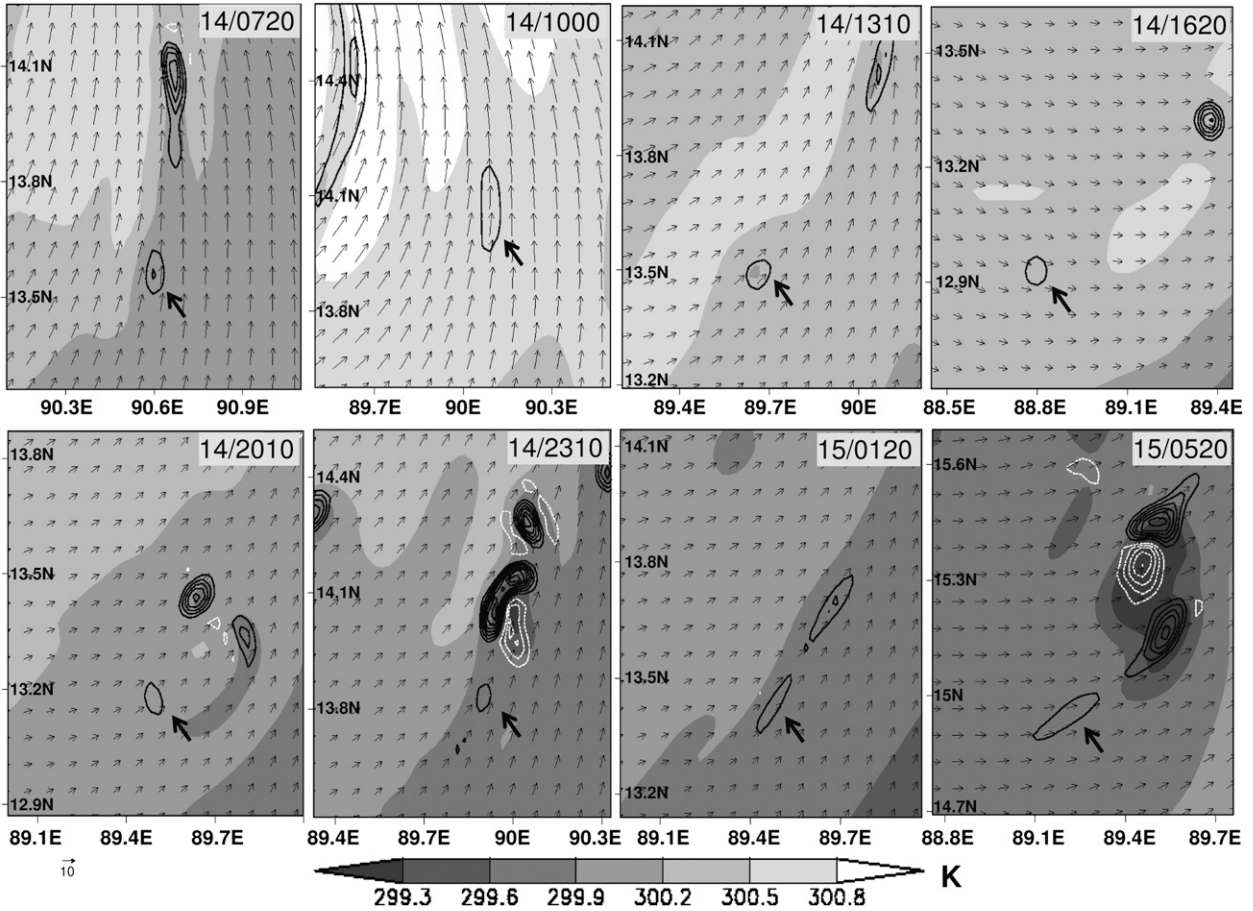
FIG. 12. Surface potential temperature (0.3-K intervals; shading), updraft (0.3 m s^{-1} intervals; black contours) at ~2-km height, and downdraft (0.3 m s^{-1} intervals; white contours) at the surface and surface wind (m s^{-1}; vector). Black arrows indicate new cells formed at different times. Date–times are (top left) 14 Nov 0720 UTC to (bottom right) 15 Nov 0520 UTC.

meridional or along-band flow gradient ($\partial v/\partial y$), which were smoothed with a 9-point smoother and averaged for the region depicted in Fig. 11a. Because $\partial v/\partial y$ was positive, indicating an increase in the meridional wind component toward the downwind (north) zone, the low-level convergence was dominated by the zonal gradient of the wind. In Fig. 15b, the zonal component of wind velocity with equivalent potential temperature (θ_e; shading) shows an inflow layer height of ~3 km on the inner side; strong wind shear limited the inflow layer height to ~2 km on the outer side. The band was developed by the low-level convergence; this convergence zone was formed by the deceleration of the cross-band flow from the inner side to the outer side of the band. The outer-side inflow dominated the convergence only within the downwind region. The magnitude of the zonal flow on the outer side of the band increased toward the downwind region and thus changed the direction of the flow from east to west. The band axis (convection line) was oriented parallel to the outer-side flow.

5. Discussion

The simulation results identified that mesoscale forcing from surface cold pools did not play a significant role in the development of the eastern rainband of Cyclone Sidr. Furthermore, the long, quasi-steady nature of a low-level convergence zone suggests that a nonuniform synoptic-scale flow was essential for convective initiation along the band. In this section, we discuss the low-level environmental flow embedding Cyclone Sidr using synoptic analysis based on observations. For this purpose, reanalyzed data from the National Centers for Environmental Prediction–National Center for Atmospheric Research (NCEP–NCAR) and data generated by the National Oceanic and Atmospheric Administration (NOAA) were used to investigate the large-scale wind field and the related environment within the Bay. In association with the synoptic-scale flows, we have further discussed the reasons for the elongation of the band and its maintenance through simulation.
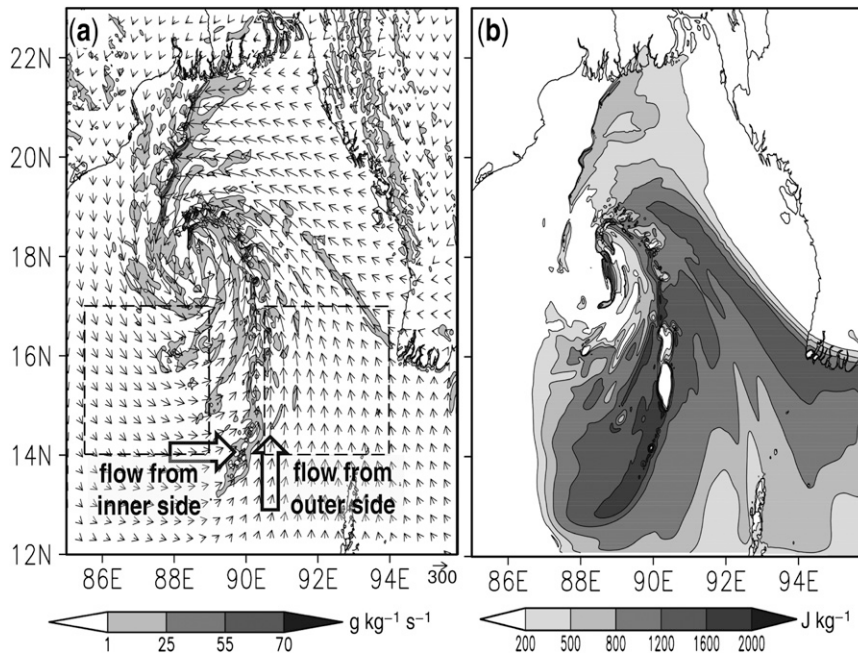
FIG. 13. (a) Shade and vector indicate surface moisture flux convergence (-10^{-3} g kg^{-1} s^{-1}) and moisture flux vector (g kg^{-1} m s^{-1}), respectively. (b) CAPE (J kg^{-1}) at 0300 UTC 15 Nov 2007. The dotted regions are used for hodographs in Fig. 14.

a. Low-level wind field in the Bay of Bengal

Cyclone Sidr formed in and advanced through the Bay of Bengal during the postmonsoon season (November). By analysis of the simulated mesoscale environment, a nonuniform, low-level wind field with an east–west moisture gradient was observed in this region during the northward movement of the cyclone. The GSM data and satellite images also show noticeable variations in wind profile and moisture fields. For further confirmation of this structure on the synoptic scale, the distribution of horizontal wind with relative humidity at 0000 UTC 15 November of the NCEP reanalysis at 925 hPa is shown in Fig. 16a. Two air flows from different environments toward the cyclone center are evident: a dry northeasterly wind and a moist east-southeasterly wind.

1) NORTHEASTERLY WIND

The contours of the mean sea level pressure for November 2007 (Fig. 16b) indicate a continental high pressure system north of the Bay. The pressure gradient force produced cool and dry northeast winds (Fig. 16c) down to the Bay; the prevailing wind was the south Indian postmonsoon wind (Rao 1963; Srinivasan and Ramamurthy 1973). The northeasterly passing over the Bay gradually gathered moisture from the sea as it became ingested into the TC circulation and began spiraling toward the cyclone center.

2) EAST-SOUTHEASTERLY WIND

The southeast region of the Bay, known as the Maritime Continent (Ramage 1968), exhibits unique topography. During the winter, active deep cumulus convections occur over the regions of Borneo, the Malay Peninsula, Sumatra, and other large Indonesian islands (Chang et al. 2005). Figure 16b confirms the maxima in convection, measured by low outgoing longwave radiation (OLR), occurring near Borneo and the surrounding ocean during November 2007. Shaik and Cleland (2008) also determined that convection was above average in the northwestern Pacific and southern Indian Ocean regions in November 2007 by analyzing OLR monthly means and anomalies over the region at 40°N–40°S, 70°E–180°. L'Heureux (2008) mentioned the existence of deep, tropical convection over tropical Indonesia using seasonal mean precipitation anomalies (October–December 2007).

This occurrence of deep convection is associated with synoptic-scale northeasterly cold surges and the Borneo vortex within the complex terrain of the Maritime Continent (Houze et al. 1981; Chang et al. 2005; Wang 2006). Chang et al. (2005) reported similar conditions, also evident in Fig. 16c, on the interaction of a synoptic-scale, low-level northeasterly with the terrain of the Malay Peninsula and Sumatra, which caused low-level convergence near Sumatra in addition to deflection of winds to
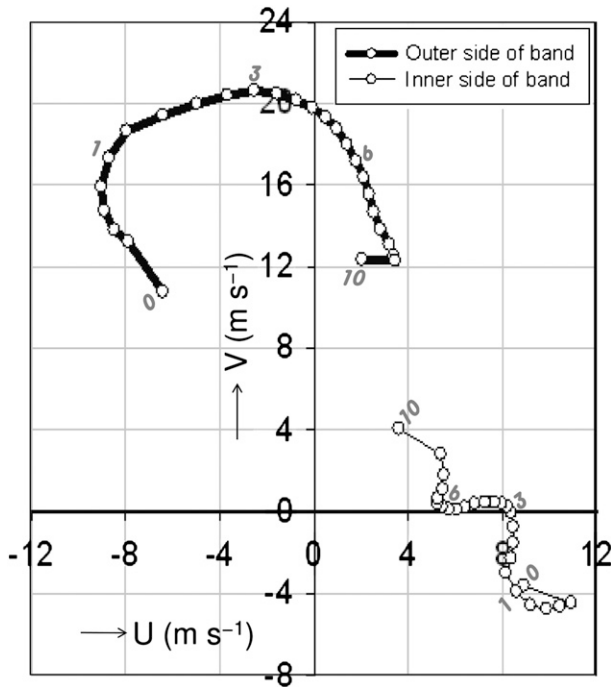
FIG. 14. Hodographs for the areas in inner and outer sides of the band, shown as dotted boxes in Fig. 13a, at 0300 UTC 15 Nov 2007. Numbers on the graph represent height in km.

the west due to terrain interference. The deflected easterly resulted in moist east-southeasterly winds extending into the Bay of Bengal, which is evident in Fig. 16d. In the figure, the southerly airflow entering the Bay during November is represented by the meridional flow at 6°N (lower boundary of the Bay of Bengal), which was anomalously large in the days preceding the cyclone.

b. Elongation and maintenance of the eastern band

Figure 17 explains the manner in which the two different low-level flows were dominated by the low pressure system of the cyclone. The contours display spatial pressure patterns with 0.5-hPa intervals above the boundary layer at ~1.6 km, which is smoothed to remove small-scale pressure perturbations. For this purpose, the Cressman (1959) weighting function was used with a 100-km radius of influence. The vectors in Fig. 17a represent wind velocity (m s^{-1}) and acceleration (m s^{-2}) of the flow; the latter of which was calculated by the vector addition of the pressure gradient force (PGF) and Coriolis force (CF). The PGF increased toward the cyclone center; as a result, the acceleration of the air parcel in the stream became stronger.

The inner and outer regions of the band (indicated in Fig. 17a) were selected for detailed examination of the low-level flow pattern and related dynamics of the horizontal wind. On the inner side of the band (west of 90°E), the

acceleration was nearly orthogonal to velocity, which suggests centripetal acceleration. The centripetal force and CF were balanced by PGF, which indicates a gradient wind balance in this region. On the contrary, the gradient wind balance was no longer maintained on the outer side of the band (east of 90°E). Here the velocity of the flow was nearly parallel to its acceleration. PGF caused the southerly flow to accelerate across the isobars. Because the PGF was stronger toward the north, the airspeed toward the cyclone center showed an increase. The discrepancies in the balance of forces between the two sides of the band are shown by three vectors of PGF, CF, and acceleration (m s^{-2}) in Figs. 17b,c. The band was formed by convergence of the gradient-balanced westerly and the nongradient-balanced southerly. As westerly flow travels along the northern and western peripheries of the cyclone, more time was available for gradient balance adjustment, whereas at the time of eastern rainband's approach, the strong southerly flow had just begun to accelerate due to the cyclone pressure gradient. The southerly flow finally assumed the curved paths to be parallel to the isobars in the downwind area.

A summary of the rainband formation with the low-level convergence of the inner- and outer-side distinct flows is shown by a conceptual model in Fig. 18. The synoptic-scale northeasterly wind was transformed into the gradient-balanced westerly in the cyclone scale through the effects of the cyclonic system. The southerly to the east of the TC converged with the westerly at low levels along the band region, which resulted in the formation of convective cells. The northward movement of the TC through the environment elongated the convergence line south of the cyclone center such that it was nearly straight rather than typically spiral (Fig. 9). The upwind straight part of the band gradually spiraled toward the center. Therefore, the horizontal structure of the eastern band was a long, quasi-straight pattern oriented parallel to the outer-side southerly flow. Our study agrees with that of Willoughby et al. (1984), which states that the outer band is formed by the movement of the vortex through the environment. Here the environment around the TC is rather nonuniform.

The gradually accelerated moist southerly supplied water vapor to the cells in the rainband. Figure 19 shows similar trends in maximum values of horizontal wind speed, water vapor, and equivalent potential temperature at a height of 100 m in the outer rainband region (91°–93°E) at 0900 UTC 15 November. The low-level wind speed increased gradually with latitude, which raised the evaporation rate from the sea surface. The northward horizontal flow containing more water vapor fed the air with higher θ_e to the cells. As a result, cellular updrafts were intensified to maintain the convection for a prolonged
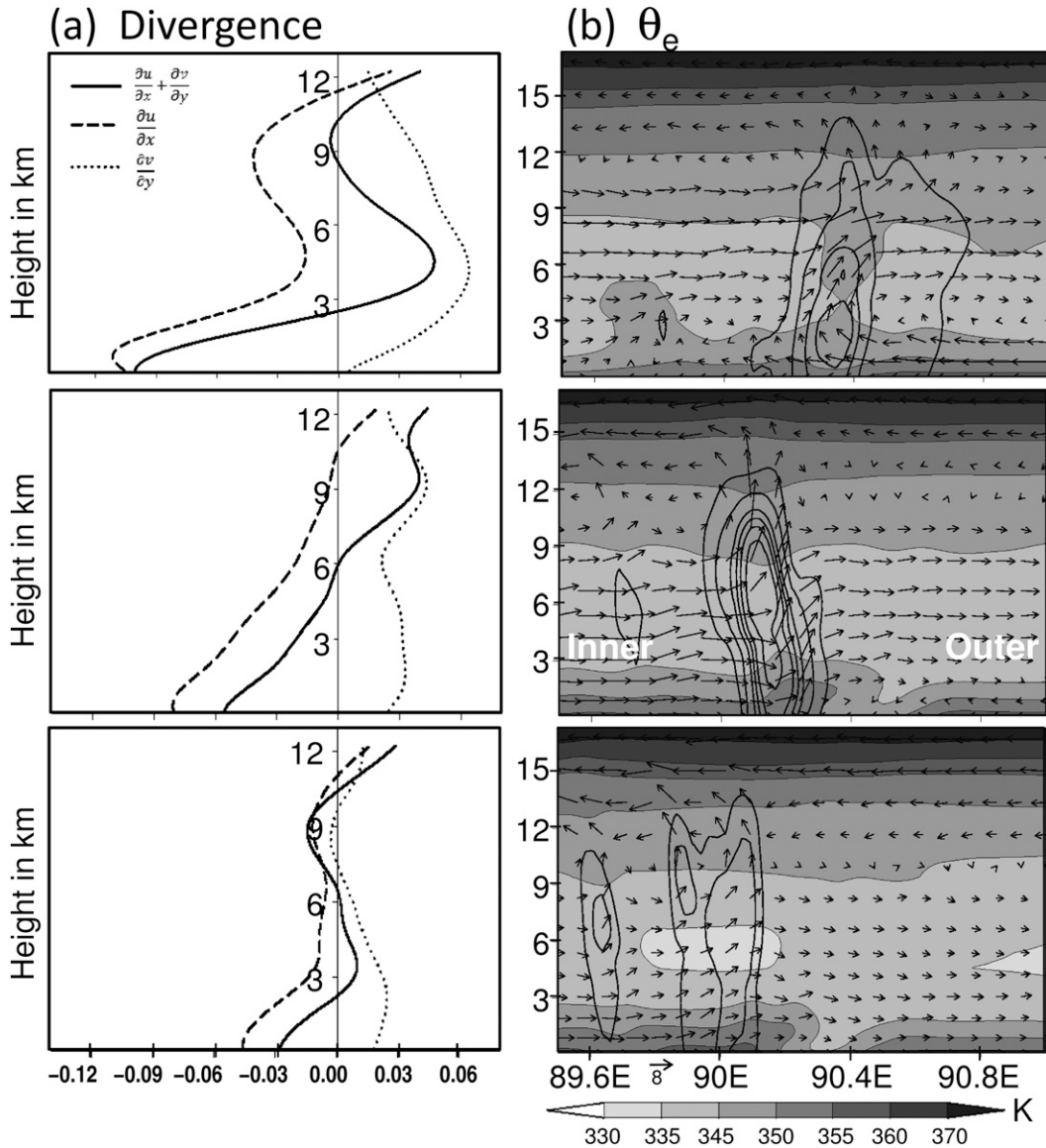
FIG. 15. (a) Divergence (solid line), zonal gradient of wind velocity (long dashed line), and meridional gradient of velocity (short dashed line); and (b) equivalent potential temperature (shading) and zonal and vertical components of wind velocity in m s^{-1} (vector) for 0600 UTC 15 Nov 2007, averaged in a manner as in Fig. 11a.

period of 1–5 h. Because of the longevity of the pre-existing cells along the convergence line, new cells were usually produced in the upwind portion of the convergence zone. Therefore, the cell production rate was continuous by the convergence with the environmental southerly flow and most cells were formed far from the cyclone center, which made the band longer than a typical TC band.

c. Differences from other TCs

Compared with other cyclones, the outer rainband of Cyclone Sidr differed in many aspects. Previous studies

noted uniform environmental flows around TCs and their influences on structure and intensity changes. The interactions between the TC and its uniform environmental flow reduced the vortex intensity by introducing vortex asymmetry resulting from surface friction, asymmetric moisture convergence and surface flux, and vertical motion (Dengler and Keyser 2000; Peng et al. 1999; Kepert 2001; Kwok and Chan 2005). However, Cyclone Sidr moved through a heterogeneous environment; air to the northwest of the TC was cool and dry, whereas that to the southeast was warm and moist.
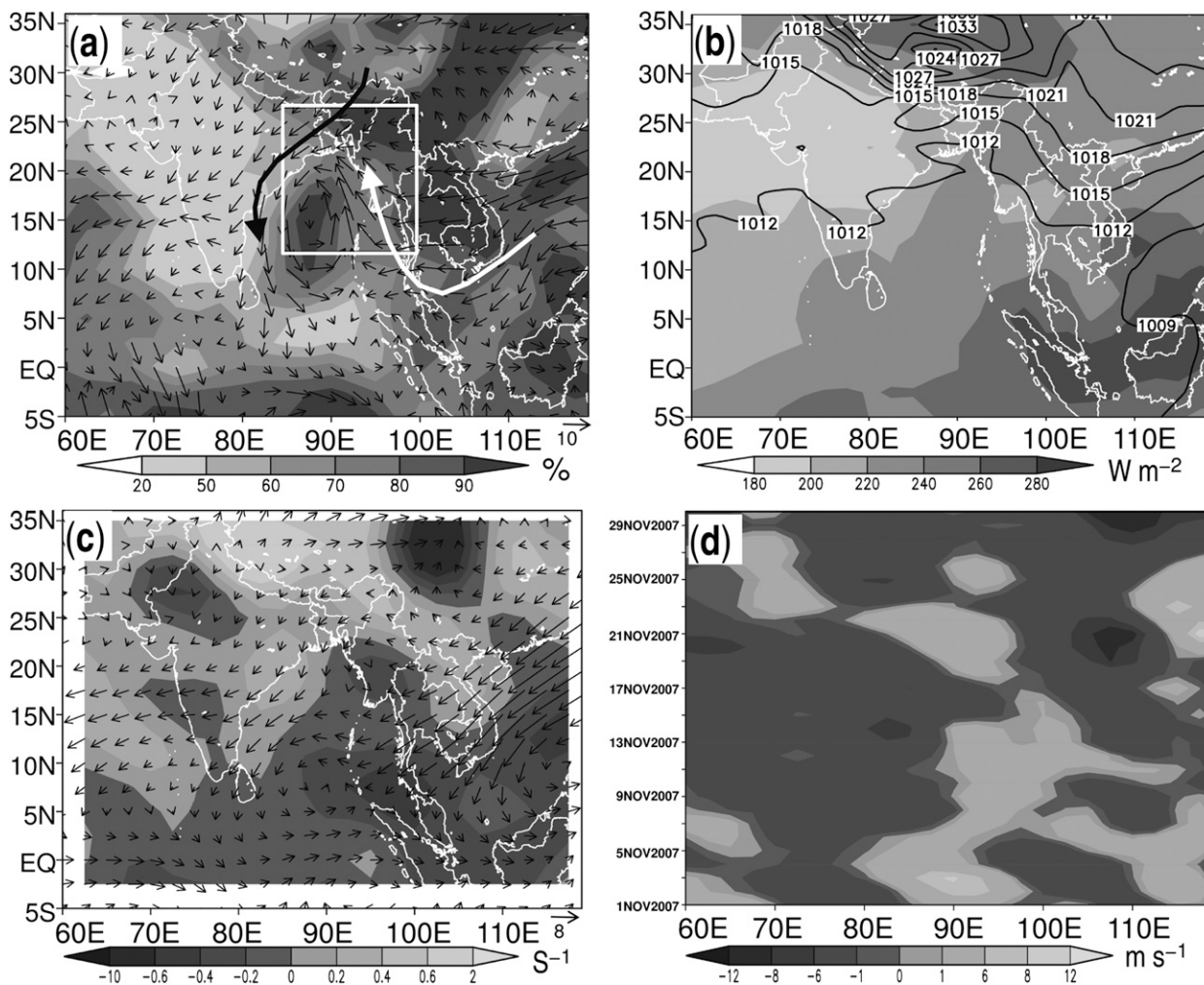
FIG. 16. (a) Relative humidity (%; shading) and horizontal wind (m s^{-1}; vector) at 0000 UTC 15 Nov 2007, obtained from NCEP reanalysis at 925 hPa. White box represents the domain of simulation. Black and white lines with arrowheads indicate dry northeasterly and moist east-southeasterly in the simulation domain, respectively. For the entire month of November 2007, (b) NOAA interpolated mean OLR (W m^{-2}, shade) and mean sea level pressure (hPa, contour), (c) 925-hPa horizontal wind (m s^{-1}; vector) and divergence of wind (s^{-1}; shading), and (d) meridional wind component (m s^{-1}) at 925 hPa.

It was previously observed that typical rainbands are prominently spiral (approximated equiangular spiral) with a maximum band length of ~400 km (e.g., Barnes et al. 1983; Willoughby et al. 1984; Powell 1990a; May 1996; Hence and Houze 2008). In contrast, Cyclone Sidr had a long, quasi-straight structure extending toward the south with a band length of ~800 km. Although the outer rainband of Hurricane Earl (1986) also had a quasi-straight shape (Powell 1990a), it was not storm stationary and was less than half the length of Cyclone Sidr's rainband.

Past studies noted the presence of deep convection in the rainband that results in the occurrence of cold pools in the boundary layer (Barnes et al. 1983; Powell 1990a,b; May 1996; Didlake and Houze 2009). The researchers determined that cold pool strength was >2 K

colder than the environment that blocks the inflow and helps to produce the new updraft along the band region. However, Ishihara et al. (1986) and Shimazu (1997) noted that no cold pool formed in the typhoon rainbands for the lifting of the surface air. In both cases, however, although the rainbands were embedded in a broad stratiform precipitation area, they did not sufficiently clarify the mechanism for new convective cell formation along the band. Ishihara et al. (1986) hypothesized that the convergence produced between the cold air ($\Delta\theta$ = 0.3–0.7 K) was associated with downdraft and the low-level warm inflow. In our study, we discovered weak ($\Delta\theta < 1$ K) and discontinuous cold air; however, these were confined within the intense mature cells with no spreading and were therefore insufficient to force the convective-scale
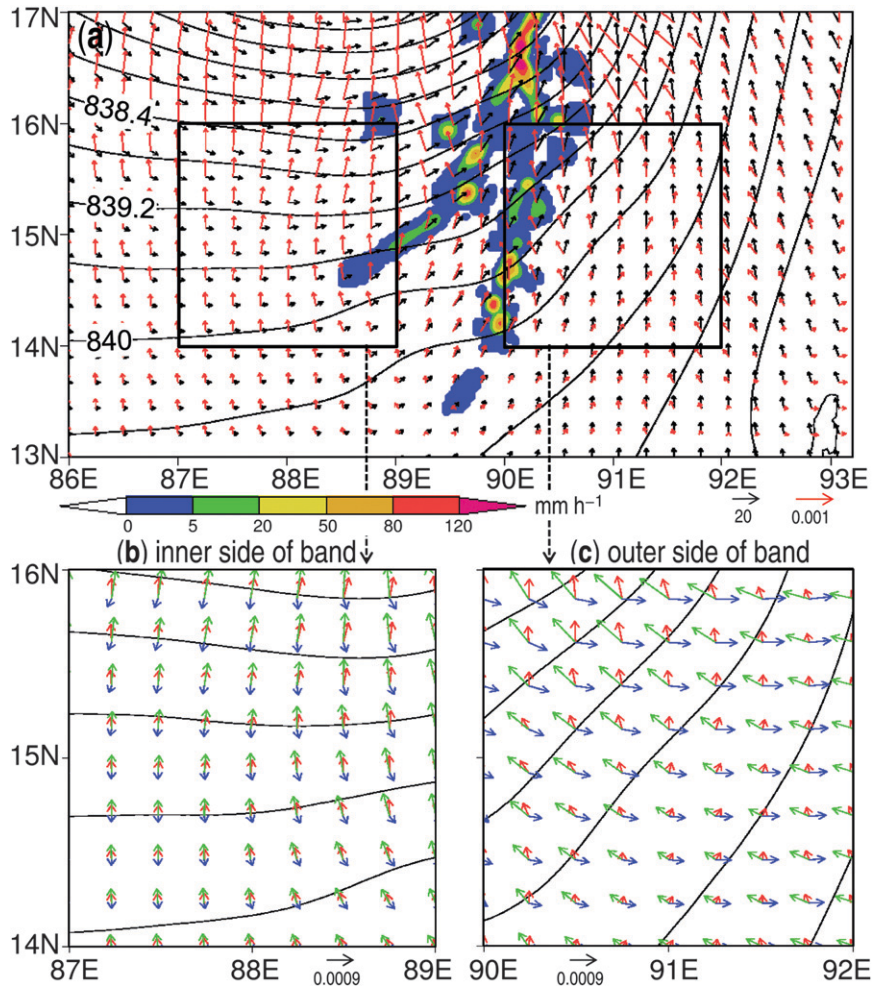
FIG. 17. (a) Contours indicate smoothed pressure at 0.4-hPa intervals at ~1.6 km; black and red vectors represent the velocity and acceleration of wind, respectively; and shading indicates the band at 0600 UTC 15 Nov 2007. (b),(c) The selected areas of (a), showing pressure gradient force (green arrows), Coriolis force (blue arrows), and acceleration (red arrows). Units are in m s^{-2}.

updrafts. The formation of convergence along the band occurred with the cross-band component of an inner-side gradient wind and an outer-side strongly sheared southerly flow within an altitude of ~3 km. The convection line (band axis) was oriented parallel to the outer-side southerly flow. Our results showed that the inflow height in the inner side was slightly deeper than that in the outer side. In contrast, Barnes et al. (1983), Powell (1990a), and May (1996) reported that the inflow of the outer side was deeper than that of the inner side.

6. Summary and conclusions

A numerical study was performed to reveal the details of the outer rainband of Cyclone Sidr, which formed

in the Bay of Bengal in 2007 and had two prominent rainbands extending in the north–south direction. The validation of the simulation using available observed data of the actual cyclone showed that the cyclone track, movement of the cyclone, its horizontal structure, and the surrounding environment were successfully simulated. The northern band was observed and simulated as a synoptic-scale front because of the presence of a strong horizontal temperature gradient northwest of Cyclone Sidr's center. The investigation of the characteristic features and formation process of the eastern band was the main objective of this study; no remarkable temperature difference near the band was observed. The following is a summary of significant findings:
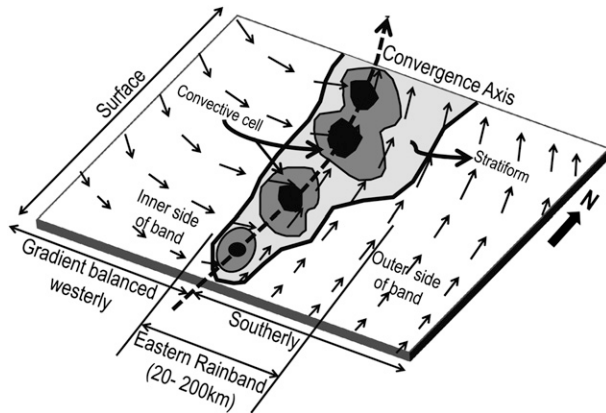
FIG. 18. Schematic of the rainband formation process of Cyclone Sidr through the convergence of two different environmental flows: a gradient-balanced westerly and a moist southerly.
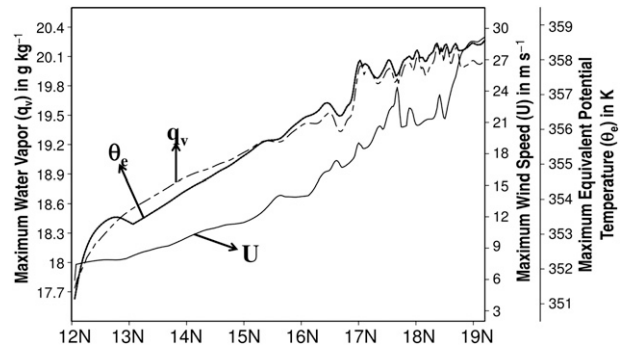

FIG. 19. Thin, thick, and dotted lines represent the maximum values of horizontal wind speed (m s^{-1}), equivalent potential temperature (K), and water vapor mixing ratio (g kg^{-1}) at 100 m, respectively, in the region of 91°–93°E at 0900 UTC 15 Nov 2007.

• Horizontal shape:

The eastern band of Cyclone Sidr was a stationary outer rainband located in the eastern side of the cyclone at a distance of ~200 km from the TC center and was oriented in the north–south direction. The length of the band gradually increased with time as the cyclone moved north, and its maximum length reached ~800 km. Its upwind shape did not follow the typical spiral pattern, but rather maintained a straight line due to the synoptic-scale forcing.

• Structure:

The band was composed of mostly independent convective cells, both ordinary and supercells, each of which had a well-defined life cycle. The upwind portion of the band was generally convective. Convective cells gradually intensified in the middle part and turned into relatively weak convection along the inner edge associated with stratiform rain along the outer edge of the band in the downwind region. As a result, the width varied in the range of 20–200 km from upwind to downwind ends. The band height at the downwind area was determined to be ~13 km and was tilted outward by the effects of the strong, clockwise vertical shear.

Cells with diameters of 10–15 km generally develop in the upwind portion of the band. However, cell production and relative position of formation with respect to the cyclone center were irregular and intermittent. Convection often initiated in regions with an MFC of $\leq -10^{-3}$ g kg^{-1} s^{-1} and CAPE with the maximum value of ~2000 J kg^{-1}. After formation, these cells moved faster than the cyclone center. Northward-moving cells merged together to form a convective cluster of ~100–200 km long in the downwind end of the band, which connected to the eyewall. North-northwest propagation of cells acted to reduce the band length. However, the band elongation occurred upwind due to the subsequent production of new cells.

• Formation process and maintenance:

In agreement with the findings of Willoughby et al. (1984), the eastern band was formed by the motion of the vortex through its surroundings. However, in this case, a nonuniform environmental flow was present around the TC. The band formed at low levels between the boundary of the inner side's weakly sheared, gradient-balanced wind and the outer side's strongly sheared, nongradient wind.

For the band formation, convective-scale downdrafts produced weak discontinuous cold pools, but the cold pools were not sufficient to produce the cell updrafts. Low-level convergence within the band was caused by the deceleration of the cross-band component of a gradient westerly ~3 km in height to a nongradient southerly ~2 km in height. The northward movement of the TC caused the convergence area to elongate gradually. The air parcel of the southerly containing water vapor gradually accelerated toward the center and fed more unstable air to the preexisting cells along the band. As a result, the updrafts were intensified, which helped to maintain the cells and the band for a longer period.

The analysis of the synoptic-scale observational evidence showed that Cyclone Sidr was embedded in two different environments within the Bay. One was related to a dry, regional northeastern Indian monsoon and the other was an east-southeastern moist wind associated with blocking and deflection by the Malay Peninsula–Sumatra terrain in the southeast region of the Bay. However, the complex interaction of synoptic-scale winds with cyclone vortex dynamics during the cyclogenesis of Cyclone Sidr is a topic for further examination.

REFERENCES

Akter, N., and K. Tsuboki, 2010: Characteristics of supercells in the rainband of numerically simulated Cyclone Sidr. *SOLA,* **6A,** 25–28.

Alam, Md. M., Md. A. Hossain, and S. Shafee, 2003: Frequency of Bay of Bengal cyclonic storms and depressions crossing different coastal zones. *Int. J. Climatol.,* **23,** 1119–1125.

Baker, A. K., M. D. Parker, and M. D. Eastin, 2009: Environmental ingredients for supercells and tornadoes within Hurricane Ivan. *Wea. Forecasting,* **24,** 223–244.

Barnes, G. M., E. J. Zipser, D. P. Jorgensen, and F. D. Marks Jr., 1983: Mesoscale and convective structure of a hurricane rainband. *J. Atmos. Sci.,* **40,** 2125–2137.

——, J. F. Gamache, M. A. LeMone, and G. J. Stossmeister, 1991: A convective cell in a hurricane rainband. *Mon. Wea. Rev.,* **119,** 776–794.

Beckman, S. K., 1990: A study of 12-h NGM low-level moisture flux convergence centers and the location of severe thunderstorms/heavy rain. Preprints, *16th Conf. on Severe Local Storms,* Kananaskis Park, Alberta, Canada, Amer. Meteor. Soc., 78–83.

Bhat, G. S., and Coauthors, 2001: BOBMEX: The Bay of Bengal Monsoon Experiment. *Bull. Amer. Meteor. Soc.,* **82,** 2217–2243.

Bunkers, M. J., 2002: Vertical wind shear associated with left-moving supercells. *Wea. Forecasting,* **17,** 845–855.

Chan, J. C. L., 2000: Tropical cyclone activity over the western North Pacific associated with El Niño and La Niña events. *J. Climate,* **13,** 997–1004.

Chang, C.-P., P. A. Harr, and H. J. Chen, 2005: Synoptic disturbances over the equatorial South China Sea and western Maritime Continent during boreal winter. *Mon. Wea. Rev.,* **133,** 489–503.

Chen, T.-C., S.-P. Weng, N. Yamazaki, and S. Kiehne, 1998: Interannual variation in the tropical cyclone formation over the western North Pacific. *Mon. Wea. Rev.,* **126,** 1080–1090.

——, S.-Y. Wang, M.-C. Yen, and W. A. Gallus Jr., 2004: Role of the monsoon gyre in the interannual variation of tropical cyclone formation over the western North Pacific. *Wea. Forecasting,* **19,** 776–785.

Cheung, N. K. W., 2006: The roles of ENSO on the occurrence of abruptly recurring tropical cyclones over the Western North Pacific Basin. *Adv. Geosci.,* **6,** 139–148.

Choudhury, A. M., 1994: Bangladesh floods, cyclones and ENSO. *Proc. Int. Conf. on Monsoon Variability and Prediction,* WCRP-84, WMO/TD-619, Vol. 1, Trieste, Italy, ICTP, 136–145.

Cressman, G. P., 1959: An operational objective analysis system. *Mon. Wea. Rev.,* **87,** 367–374.

Das, P. K., 1968: *The Monsoons.* National Book Trust of India, 252 pp.

Dengler, K., and D. Keyser, 2000: Intensification of tropical-cyclone like vortices in uniform zonal background-flows. *Quart. J. Roy. Meteor. Soc.,* **126,** 549–568.

Didlake, A. C. Jr., and R. A. Houze Jr., 2009: Convective-scale downdrafts in the principal rainband of Hurricane Katrina (2005). *Mon. Wea. Rev.,* **137,** 3269–3293.

Diercks, J. W., and R. A. Anthes, 1976: Diagnostic studies of spiral rain bands in a nonlinear hurricane model. *J. Atmos. Sci.,* **33,** 959–975.

Dvorak, V., 1975: Tropical cyclone intensity analysis and forecasting from satellite imagery. *Mon. Wea. Rev.,* **103,** 420–430.

Eastin, M. D., T. L. Gardner, M. C. Link, and K. C. Smith, 2012: Surface cold pools in the outer rainbands of Tropical Storm Hanna (2008) near landfall. *Mon. Wea. Rev.,* **140,** 471–491.

Engerer, N. A., D. J. Strensrud, and M. C. Coniglio, 2008: Surface characteristics of observed cold pools. *Mon. Wea. Rev.,* **136,** 4839–4849.

Harr, P. A., and J. C. L. Chan, 2005: Monsoon impacts on tropical cyclone variability. *The Global Monsoon System: Research and Forecast,* C.-P. Chang, B. Wang, and N.-C. G. Lau, Eds., WMO, 512–542.

Hasegawa, K., 2008: Features of super cyclone Sidr to hit Bangladesh in Nov 07 and measures for disaster from results of JSCE investigation. *Proc. WFEO-JFES-JSCE Joint Int. Symp. on Disaster Risk Management,* Sendai, Japan, Science Council of Japan, 51–58.

Hence, D. A., and R. A. Houze Jr., 2008: Kinematic structure of convective-scale elements in the rainbands of Hurricanes Katrina and Rita (2005). *J. Geophys. Res.,* **113,** D15108, doi:10.1029/2007JD009429.

Houze, R. A. Jr., S. G. Geotis, F. D. Marks, and A. K. West, 1981: Winter monsoon convection in the vicinity of North Borneo. Part I: Structure and time variation of the clouds and precipitation. *Mon. Wea. Rev.,* **109,** 1595–1614.

Ishihara, M., Z. Yanagisawa, H. Sakakibara, K. Matsuura, and J. Aoyagi, 1986: Structure of a typhoon rainband observed by two Doppler radars. *J. Meteor. Soc. Japan,* **64,** 923–939.

Kepert, J. D., 2001: The dynamics of boundary layer jets within the tropical cyclone core. Part I: Linear theory. *J. Atmos. Sci.,* **58,** 2469–2484.

Koch, S. E., and J. McCarthy, 1982: The evolution of an Oklahoma dryline. Part II: Boundary-layer forcing of mesoconvective systems. *J. Atmos. Sci.,* **39,** 237–257.

Krishna, K. M., 2008: Intensifying tropical cyclones over the North Indian Ocean during summer monsoon—Global warming. *Global Planet. Change,* **65,** 12–16.

Kurihara, Y., 1976: On the development of spiral bands in a tropical cyclone. *J. Atmos. Sci.,* **33,** 940–958.

Kwok, H. Y., and J. C. L. Chan, 2005: The influence of uniform flow on tropical cyclone intensity change. *J. Atmos. Sci.,* **62,** 3193–3212.

L'Heureux, M., 2008: An overview of the 2007-08 La Niña and boreal wintertime variability. *Extended Abstracts, 33rd NOAA Annual Climate Diagnostics and Prediction Workshop,* Lincoln, NE, Science and Technology Infusion Climate Bulletin, 1–8.

Liu, A. Q., G. W. K. Moore, K. Tsuboki, and I. A. Renfrew, 2004: A high resolution simulation of convective roll clouds during a

cold-air outbreak. *Geophys. Res. Lett.,* **31,** L03101, doi:10.1029/2003GL018530.

Louis, J. F., M. Tiedtke, and J. F. Geleyn, 1981: A short history of the operational PBL parameterization at ECMWF. *Proc. ECMWF Workshop on Planetary Boundary Layer Parameterization,* Reading, United Kingdom, ECMWF, 59–79.

Maesaka, T., G. W. K. Moore, Q. Liu, and K. Tsuboki, 2006: A simulation of a lake effect snowstorm with a cloud resolving numerical model. *Geophys. Res. Lett.,* **33,** L20813, doi:10.1029/2006GL026638.

May, P. T., 1996: The organization of convection in the rainbands of tropical cyclone Laurence. *Mon. Wea. Rev.,* **124,** 807–815.

——, and G. J. Holland, 1999: The role of potential vorticity generation in tropical cyclone rainbands. *J. Atmos. Sci.,* **56,** 1224–1228.

McCaul, E. W., Jr., 1991: Buoyancy and shear characteristics of hurricane–tornado environments. *Mon. Wea. Rev.,* **119,** 1954–1978.

——, and M. L. Weisman, 1996: Simulations of shallow supercell storms in landfalling hurricane environments. *Mon. Wea. Rev.,* **124,** 408–429.

——, and ——, 2001: The sensitivity of simulated supercell structure and intensity to variations in the shapes of environmental buoyancy and shear profiles. *Mon. Wea. Rev.,* **129,** 664–687.

Mukhopadhyay, P., and S. C. Dutta, 2007: A reconnaissance based vulnerability and damage survey report at the Sagar Island, West Bengal: Effect of the Cyclone Sidr of 15th November, 2007. Bengal Engineering and Science University, Shibpur, India, 22 pp.

Murata, A., K. Saito, and M. Ueno, 2003: The effects of precipitation schemes and horizontal resolution on the major rainband in typhoon Flo (1990) predicted by the MRI mesoscale nonhydrostatic model. *Meteor. Atmos. Phys.,* **82,** 55–73.

Nasuno, T., and M. Yamasaki, 1997: The effect of surface friction on the mesoscale organization of cumulus convection in tropical cyclones. *J. Meteor. Soc. Japan,* **75,** 907–924.

Negri, A. J., and T. H. Vonder Haar, 1980: Moisture convergence using satellite-derived wind fields: A severe local storm case study. *Mon. Wea. Rev.,* **108,** 1170–1182.

Ohigashi, T., and K. Tsuboki, 2007: Shift and intensification processes of the Japan-Sea Polar-Airmass Convergence Zone associated with the passage of a mid-tropospheric cold core. *J. Meteor. Soc. Japan,* **85,** 633–662.

Ostby, F. P., 1975: An application of severe storm forecast techniques to the outbreak of June 8, 1974. Preprints, *Ninth Conf. on Severe Local Storms,* Norman, OK, Amer. Meteor. Soc., 7–12.

Peng, M. S., B.-F. Jeng, and R. T. Williams, 1999: A numerical study on tropical cyclone intensification. Part I: Beta effect and mean flow effect. *J. Atmos. Sci.,* **56,** 1404–1423.

Petterssen, S., 1956: *Motion and Motion Systems.* Vol. 2, *Weather Analysis and Forecasting,* McGraw-Hill, 428 pp.

Powell, M. D., 1990a: Boundary layer structure and dynamics in outer hurricane rainbands. Part I: Mesoscale rainfall and kinematic structure. *Mon. Wea. Rev.,* **118,** 891–917.

——, 1990b: Boundary layer structure and dynamics in outer hurricane rainbands. Part II: Downdraft modification and mixed layer recovery. *Mon. Wea. Rev.,* **118,** 918–938.

Ramage, C. S., 1968: Role of a tropical "Maritime Continent" in the atmospheric circulation. *Mon. Wea. Rev.,* **96,** 365–370.

Rao, K. V., 1963: A study of the Indian northeast monsoon season. *Indian J. Meteor. Geophys.,* **14,** 143–155.

Roca, R., and V. Ramanathan, 2000: Scale dependence of monsoonal convective systems over the Indian Ocean. *J. Climate,* **13,** 1286–1298.

Rogash, J. A., and R. D. Smith, 2000: Multiscale overview of a violent tornado outbreak with attendant flash flooding. *Wea. Forecasting,* **15,** 416–431.

Ryan, B. F., G. M. Barnes, and E. J. Zipser, 1992: A wide rainband in a developing tropical cyclone. *Mon. Wea. Rev.,* **120,** 431–447.

Sakurai, T., K. Yukio, and T. Kuragano, 2005: Merged satellite and in-situ data global daily SST. *Proc. IGARSS 2005 IEEE Int. Geoscience and Remote Sensing Symp.,* Vol. 4, Seoul, South Korea, Geoscience and Remote Sensing Society, 2606–2608.

Senn, H. V., H. W. Hiser, and R. C. Bourret, 1957: Studies of hurricane spiral bands as observed on radar. Final Rep., U.S. Weather Bureau, Contract Cwb-9066, University of Miami, 21 pp.

Shaik, H. A., and S. J. Cleland, 2008: The tropical circulation in the Australian/Asian region – November 2007 to April 2008. *Aust. Meteor. Mag.,* **55,** 367–378.

Shankar, D., P. N. Vinayachandran, A. S. Unnikrishnan, and S. R. Shetye, 2002: The monsoon currents in the north Indian Ocean. *Prog. Oceanogr.,* **52,** 63–119.

Shimazu, Y., 1997: Wide slow-moving rainbands and narrow fast-moving rainbands observed in Typhoon 8913. *J. Meteor. Soc. Japan,* **75,** 67–80.

Singh, O. P., T. M. Ali Khan, and Md. S. Rahman, 2000: Changes in the frequency of tropical cyclones over the North Indian Ocean. *Meteor. Atmos. Phys.,* **75,** 11–20.

Skwira, G. D., J. L. Schroeder, and R. E. Peterson, 2005: Surface observations of landfalling hurricane rainbands. *Mon. Wea. Rev.,* **133,** 454–465.

Srinivasan, V., and K. Ramamurthy, 1973: Northeast monsoon. Indian Meteorological Department. Rep. FMU IV-18.4, 132 pp.

Tabata, A., H. Sakakibara, M. Ishihara, K. Matsuura, and Z. Yanagisawa, 1992: A general view of the structure of typhoon 8514 observed by dual-Doppler radar—From outer rainbands to eyewall clouds. *J. Meteor. Soc. Japan,* **70,** 897–917.

Tsuboki, K., and A. Sakakibara, 2002: Large-scale parallel computing of cloud resolving storm simulator. *High Performance Computing,* H. P. Zima et al., Eds., Springer, 243–259.

——, and ——, 2007: Numerical prediction of high-impact weather systems—The text book for Seventeenth IHP training course in 2007. HyARC, Nagoya University, Japan, and UNESCO, 273 pp.

Ulanski, S. L., and M. Garstang, 1978: The role of surface divergence and vorticity in the life cycle of convective rainfall. Part I: Observation and analysis. *J. Atmos. Sci.,* **35,** 1047–1062.

van Zomeren, J., and A. van Delden, 2007: Vertically integrated moisture flux convergence as a predictor of thunderstorms. *Atmos. Res.,* **83,** 435–445.

Wang, B., 2006: *The Asian Monsoon.* Springer and Praxis Publishing Co., 787 pp.

——, and J. C. L. Chan, 2002: How strong ENSO events affect tropical storm activity over the western North Pacific. *J. Climate,* **15,** 1643–1657.

Wang, C.-C., G.T.-J. Chen, T.-C. Chen, and K. Tsuboki, 2005: A numerical study on the effects of Taiwan topography on a convective line during the mei-yu season. *Mon. Wea. Rev.,* **133,** 3217–3242.

Wang, Y., 2002a: Vortex Rossby waves in a numerically simulated tropical cyclone. Part II: The role in tropical cyclone structure and intensity changes. *J. Atmos. Sci.,* **59,** 1239–1262.

——, 2002b: An explicit simulation of tropical cyclones with a triply nested movable mesh primitive equation model: TCM3. Part

II: Model refinements and sensitivity to cloud microphysics parameterization. *Mon. Wea. Rev.,* **130,** 3022–3036.

——, 2009: How do outer spiral rainbands affect tropical cyclone structure and intensity? *J. Atmos. Sci.,* **66,** 1250–1273.

Weisman, M. L., and J. B. Klemp, 1984: The structure and classification of numerically simulated convective storms in directionally varying wind shears. *Mon. Wea. Rev.,* **112,** 2479–2498.

Willoughby, H. E., 1978: A possible mechanism for the formation of hurricane rainbands. *J. Atmos. Sci.,* **35,** 836–848.

——, J. A. Clos, and M. G. Shoreibah, 1982: Concentric eyewalls, secondary wind maxima, and the evolution of the hurricane vortex. *J. Atmos. Sci.,* **39,** 395–411.

——, F. D. Marks, and R. J. Feinberg, 1984: Stationary and moving convective bands in hurricanes. *J. Atmos. Sci.,* **41,** 3189–3211.

Yamada, H., 2008: Numerical simulations of the role of land surface conditions in the evolution and structure of summertime thunderstorms over a flat highland. *Mon. Wea. Rev.,* **136,** 173–188.

Yamasaki, M., 1983: A further study of the tropical cyclone without parameterizing the effects of cumulus convection. *Pap. Meteor. Geophys.,* **34,** 221–260.

Zipser, E. J., 1977: Mesoscale and convective-scale downdrafts as distinct components of squall-line circulation. *Mon. Wea. Rev.,* **105,** 1568–1589.

Zuidema, P., 2003: Convective clouds over the Bay of Bengal. *Mon. Wea. Rev.,* **131,** 780–798.